

MeqSilhouette : a mm-VLBI observation and signal corruption simulator

Dissertation presented in fulfillment of the requirements for the
degree of
MASTER OF SCIENCE
in the Department of Physics and Electronics,
Rhodes University

Supervisors:

Author:

Tariq BLECHER

Dr. Roger DEANE

Dr. Gianni BERNARDI

Prof. Oleg SMIRNOV

December 2016

Abstract

The Event Horizon Telescope (EHT) aims to spatially resolve the silhouette (or shadow) of the supermassive black holes in the Galactic Centre (Sgr A \star) and M87. The primary scientific objectives are to test general relativity in the strong-field regime and to probe accretion and jet-launch physics at event-horizon scales. This is made possible by the technique of Very Long Baseline Interferometry (VLBI) at (sub)millimetre wavelengths, which can achieve angular resolutions of order $\sim 10 \mu\text{-arcsec}$. However, this approach suffers from unique observational challenges, including scattering in the troposphere and interstellar medium; rapidly time-variable source structure in both polarized and total intensity; as well as non-negligible antenna pointing errors. In this, the first paper in a series, we present the MEQSILHOUETTE software package which is specifically designed to accurately simulate EHT observations. It includes realistic descriptions of a number of signal corruptions that can limit the ability to measure the key science parameters. This can be used to quantify calibration requirements, test parameter estimation and imaging strategies, and investigate systematic uncertainties that may be present. In doing so, a stronger link can be made between observational capabilities and theoretical predictions, with the goal of maximising scientific output from the upcoming order of magnitude increase in EHT sensitivity.

Acknowledgements

Plagiarism

I acknowledge that plagiarism is wrong and hereby declare that the work contained in this document and in the supporting software is my own, save for that which is properly acknowledged.

Tariq Dylan Blecher

Source code repo and license,
accessibility etc

Contents

Abstract	ii
Acknowledgements	iii
Plagiarism	iv
1 Introduction	1
1.1 Unsolved questions in black hole astrophysics	1
1.1.1 Innermost accretion and jet launch mechanisms	4
1.1.2 Measuring space-time in strong gravity	5
1.2 Cranking up the angular resolution	6
1.3 The Event Horizon Telescope	8
1.3.1 Overview	8
1.4 A realistic mm-VLBI simulator	10
1.5 Outline	13
2 Theory	17
2.1 Radio Interferometry	17
2.1.1 Measurement Equation	17
2.1.2 Self-calibration and fringe-fitting	22
2.1.3 mm-VLBI observables and data products	23
2.1.4 Variability and the static source assumption	24
2.2 Signal Corruptions	26
2.2.1 Scattering basics	27

2.2.2	Interstellar medium scattering	30
2.2.3	Troposphere	36
2.2.4	Instrumental	46
3	Software implementation	49
3.1	Design objectives	49
3.2	Architechture and Workflow	50
3.2.1	ISM scattering	54
3.2.2	Atmospheric corruption simulator	55
3.2.3	Pointing error simulator	56
3.3	RODRIGUES interface	57
4	Results and analysis	58
4.1	Canonical simulations	58
4.1.1	ISM	58
4.1.2	Atmospheric	59
4.1.3	Pointing	65
4.2	Calibration and imaging of a time variable source in the presence of the troposphere	65
5	Conclusion and future work	66
	Bibliography	80

List of Figures

¹<http://armchairastronautics.blogspot.co.za/p/space-observatories.html>

1.3 (Image credit: Remo Tilanus) The view of the Event Horizon Telescope (EHT) from Sgr A*. This interferometric array uses Earth-diameter baselines, operating at 230 – 345 GHz to attain an angular resolution of the order of $\theta_{\text{res}} \sim 10 \mu\text{-arcsec}$. Baselines to ALMA are shown in red, to highlight its order of magnitude higher sensitivity. Note that the CARMA station has recently been decommissioned, a telescope in Greenland is currently being constructed and there is ongoing investigation into a possible site on the African continent.	16
2.1	21
2.2 Illustration depicting the basics of scattering in the weak (left) and strong (right) regimes. In the weak regime, the signal is coherently propagated over an area, $A_{\text{weak}} \approx \pi r_F^2$, whereas in the strong regime, coherent propagation is split over many areas, each of size $A_{\text{strong}} \approx \pi r_0^2$	29
2.3 The λ^2 dependence of scattering kernel size is shown by the solid line. This has been derived from measurements made at $\lambda > 17$ cm Bower et al. [2006]. The dotted line shows the derived intrinsic source size which scales as $\lambda^{1.44}$. This was derived from measurements in the wavelength range, $2 \text{ cm} < \lambda < 1.3 \text{ mm}$ [Doeleman et al., 2008]. The red circles show major-axis observed sizes of Sgr A* and the green points show the derived intrinsic major-axis size. This plot was reproduced from Doeleman et al. [2008].	31
2.4 Closure phases recorded in a VLBA + LMT observation of Sgr A* at $\lambda = 3.5 \text{ mm}$?. The data points are shown as red circles and blue squares and are only distinguished by the calibrator used. The green envelopes show the 1σ closure phase prediction induced by scattering-induced substructure. Reproduced from ?.	35

- 2.5 Recorded zenith absorption spectrum in the 160 – 520 GHz range, taken on Mauna Kea at an altitude of ≈ 4000 m. The data has been fit to a sum of H₂O lines, an H₂O pseudo-continuum and dry absorption lines. The model has been generated using the ATM code (see section 2.2.3), with the bottom panel showing the residuals. Here ‘dry’ refers to all atmospheric constituents except H₂O. Reproduced from Pardo et al. [2001] 39
- 2.6 A log-log plot of RMS visibility phase versus baseline length for an observation of 1 Jy source 0748 + 240 with VLA at 22 GHz over a 90 min duration. The open circles show RMS phase as measured whereas the solid squares show the same values with a constant thermal noise contribution of 10° subtracted in quadrature. Note that the measured and theoretical Kolmogorov turbulent exponent β changes with distance on the phase screen as the viewing configuration transitions from a thick screen ($\beta_{\text{theory}} = 5/3$) to a thin screen ($\beta_{\text{theory}} = 2/3$) at $r \approx 1$ km and from a thin screen to completely uncorrelated regime ($\beta = 0$) beyond the outer scale at $r \approx 6$ km. Although these regimes appear distinct, there is continuous variation between them. Reproduced from Carilli and Holdaway [1997] 44
- 3.1 Flow diagram showing basic sequence of a MEQ SILHOUETTE simulation pipeline. The specific sequence is determined by the driver script whereas the logic of each step is contained in an object-oriented framework. The details of the station information, observation strategy, tropospheric and ISM conditions are specified in a user-defined input configuration file. The pipeline is extendable, allowing any additional, arbitrary Jones matrices to be incorporated. 52

- 4.1 An example simulation of ISM scattering towards Sgr A*, observed with SMT-JCMT-CARMA. The top panel, left to right, shows the original FWHM = 40 μ -arcsec Gaussian (**top left**), the simulated ISM scattered image on the first night (**top middle**) and last night (**top right**) of the observation, respectively. The bottom panel, left to right, shows the evolution of the 10 minute-averaged closure phase with epoch (**bottom left**), *uv*-tracks for each night (**bottom middle**) and the RMS fractional visibility amplitude differences $\sigma_{\Delta V/V_{ea}}$ as a function of *uv*-distance (**bottom right**). $\Delta V = (|V_a| - |V_{ea}|)$, where $|V_a|$ and $—|V_{ea}|$ are the simulated average and ensemble average visibility amplitudes respectively. Variations from the ensemble-average flux on the shortest baselines reveal total flux modulation while flux variations on longer baselines and non-zero closure phases track the fluctuations in substructure. Furthermore, ISM scattering simulations can constrain the variability fraction associated with the screen, enabling a more robust estimation of source variability, as demonstrated in Ortiz-León et al. [2016]. The time-variability of the ISM is built into the MEQSILHOUETTE framework. 60
- 4.2 Simulated mean opacity (black) and sky brightness temperature (red) at $\nu = 230$ GHz for three typical ground pressures and temperatures over a typical PWV range [Lane, 1998] which approximately represent the sites of SPT (dots), ALMA (squares) and SMA (triangles). The legend shows the estimated input ground (pressure, temperature) parameters for each site. 61

4.3 Simulation of the total delay (left) and the turbulent atmospheric delay (right) for SMA (blue) and ALMA (green) sites towards Sgr A*. Ground pressures and temperatures are the same as Fig. 4.2, precipitable water vapour above each station is set to $w = 2$ mm, and the instantaneous zenith coherence time is set $T_0 = 10$ s for both stations. Note that all tropospheric parameters are, however, independently set. The conversion from time delay to phase at 230 GHz is 1 rad = 0.7 ps. 62

4.4 The effect of residual troposphere phase noise on interferometric images of a point source observed for 12 hours at 230 GHz with 4 GHz bandwidth with the following array : SPT, ALMA, SMA, SMT, LMT and JCMT, assuming the same SEFDs as Lu et al. [2014] and an elevation limit of 15° . For simplicity the weather parameters at each station were set to: coherence time $t_0 = 10$ sec; PWV depth $w = 1$ mm; ground pressure $P = 600$ mb; ground temperature $T = 273$ K. **Top left:** interferometric map with thermal noise only. **Top right:** atmospheric attenuation and sky noise (due to non-zero opacity) with 1% of the turbulent phase noise added. **Bottom left:** as previous but with 3% of turbulent phase contribution. **Bottom right:** as previous but with 6% turbulent phase contribution. The fractional turbulent phase contributions are illustrative of the effect of fringe-fitting errors. Note the decrease in the source peak flux with increasing turbulent tropospheric phase noise. Note further that the peak source centroid is offset from its true position (black crosshairs). 63

4.5 RMS relative amplitude error induced by pointing error with the 50 m (i.e. fully illuminated) LMT antenna as a function of pointing error offset ρ at 230 GHz. We assume that these errors are degenerate or non-separable from the self-calibration/fringe-fitting model used. See text for the description of the three models used. This simulation capability enables constraints on the magnitude of pointing-induced errors given a particular pointing calibration strategy.	64
--	----

List of Tables

2.1 A re-analysis of VLBI observations of Sgr A* by Psaltis et al. [2015] has yielded revised estimates of the parameters associated with the Gaussian scattering kernel. Note that the position angle is measured East of North.	32
3.1 The list of the parameters, aside from the source model, needed to initialise and run SCATTERBRANE. Time variability is made possible as N_{pix} can be a 2-tuple (i.e. a rectangular screen can be created).	54

Chapter 1

Introduction

1.1 Unsolved questions in black hole astrophysics

Black Holes (BHs) are both extreme and ubiquitous objects which are increasingly becoming seen as central to our understanding of the physical universe. The first inferences of their existence [date + chandreskar,Schwarschild etc.]came from the observations of the highly energetic Active Galactic Nucleus (AGN) Cygnus A as well as the rapid variability of quasars, both implying a massive and compact engine [?, and references therein]. Since then, [rather key questions, will focus on accretion later] the case for accretion onto a BH powering highly energetic events such as kiloparsec-scale jets and gamma ray bursts have strengthened considerably, however the mechanisms by which these observables are produced within the range of accreting black hole systems is still highly debated. We now introduce some basic black hole properties, followed by a several key questions in black hole astrophysics. Later in this chapter we present a unique but challenging observation which could potentially answer several of these questions and subsequently how this work can aid this objective.

BHs are formed through the gravitational collapse of a stellar core during

a supernovae explosion or from direct collapse from a primordial gas cloud and can grow in mass through accretion of nearby material and/or mergers with other black holes. The observed BH mass distribution is separated into two distinct mass classes, stellar and supermassive - the former with mass on the order $M \sim 10M_{\odot}$ and the latter $M \sim 10^6 - 10^{10}M_{\odot}$ [Falcke and Markoff, 2013]. Here we will focus on the class of supermassive black holes (SMBHs) for reasons provided shortly.

SMBHs form and reside (unless ejected) in the centres of all galaxies [?]. Observations of their surrounding galactic bulges show tight correlations between BH mass and the bulge luminosity and stellar velocity dispersion [??], suggesting coevolution or feedback processes. The role of SMBHs in galaxy evolution and in the evolution of structure in the universe in general [?], and hence those topics themselves[word-what are you trying to say] can only be fully understood if the fundamental black hole processes is central to understanding the physical universe.

Accretion of gas from large radii requires removal of both angular momentum and gravitational energy.? The processes which release these quantities result in radiation, jet and wind outflows. parameters of accretion : M,a,mdot,edd,gas properties as large r, empirical 'efficiency' of accretion. Treating the black hole engine as a black box,[it's nice - carry it all] The dominant emission mechanism is synchrotron. [yes, and broad powerlaw spectrum and linearly polarised emission.

microphysics uncertain. differential rotation - source of energy, turns into MRI which can grow mag field and create turbulence

[feed in to above] Considering the physical processes around a BH as a black box scenario, accretion of gas onto a SMBH releases gravitational energy and angular momentum. Output from this process is radiation, jet and winds The classical idea of an Active Galactic Nucleus (AGN) is a SMBH surrounded by an accretion disc ejecting a jet along it's polar axis. The jets can remain collimate over large cosmic distances. magnetic fields

The past half century has seen significant advances in BH theory and

observation, however key questions remain unsolved - until now perhaps.[i think i've said this already - rather do specifics than such general terms] However much of the work on black holes emission mechanisms and dynamics remain inconclusive as no observation has yet been able to resolve the AGN at it's core. Hence the need for direct ofr resolved observations o [fnish sentence]

To constrain the physics near a black hole, the observation needs to be sensitive to scales comparable to the event horizon. For a non-spinning (Schwarschild) black hole, the event horizon is spherically symmetric with a radius,

$$R_{\text{Sch}} = 2GM_{\text{BH}}/c^2, \quad (1.1)$$

where M_{BH} is the black hole mass, G is the gravitational constant and c is the speed of light. The angular size of such an event horizon in the far-field approximation is

$$\theta_{\text{Sch}} = R_{\text{Sch}}/d_{\text{src}} \quad (1.2)$$

$$\approx 0.02'' \times 10^{-9} (M_{\text{BH}}/M_{\odot}) (\text{kpc}/d_{\text{src}}), \quad (1.3)$$

where d_{src} is the distance from observer to source.

[The best candidate is obviously.., a line or two about SgrA discovery] For Sgr A*, optical/infrared monitoring of stars orbiting Sgr A* [Gillessen et al., 2009] has yielded $M_{\text{BH}} = 4.30 \pm 0.36 \times 10^6 M_{\odot}$ and $d_{\text{src}} = 8.28 \pm 0.32$ kpc which results in $\theta_{\text{Sch}} \approx 10 \mu\text{-arcsec}$.

[send the next two paragraphs to EHT section?] There are other important reasons why this observation needs to be conducted near sub-millimetre frequencies. Firstly, the spectral energy distribution of Sgr A* peaks sharply in sub-millimetre, which for a self-absorbed synchrotron source implies that the emission becomes optically thin and at these frequencies, that the emission arises from event horizon scales [Serabyn et al., 1997, Falcke et al., 1998]. Hence observations at the sub-millimetre are sensitive to the innermost emis-

sion.

The second reason is that blurring effects, induced by scattering in the Interstellar Medium (ISM) in the direction of the Galactic Centre [e.g. Fish et al., 2014] fall as ν^{-2} and become subdominant to intrinsic structure in the sub-millimetre range.

1.1.1 Innermost accretion and jet launch mechanisms

[HOW IS ENERGY TRANSPORTED/REMOVED? HOW IS ANGULAR MOMENTUM TRANSFERRED? LOST]

extracting the rotational energy from the black hole fundamental plane of black hole activity - accretion rate and black hole mass seems to determine jet power however theory suggests that spin should power the jet In addition to probing the spacetime around black holes, the EHT will also enable unprecedented observations of the inner accretion and jet physics, the exact mechanisms and contexts of which are highly debated.

Radiatively Inefficient Accretion Flow [(RIAF), ??] models offer a popular explanation for the $\sim 10^{-8}L_{\text{edd}}$ of Sgr A*, however horizon scale observations are still needed to robustly compare models. In this model the electron and proton temperatures decouple due to the low density of the gas. Most of the gravitational energy is converted into the viscous thermal energy of protons which radiate inefficiently compared to electrons. The protons are then either advected into the SMBH or ejected via outflows possibly in the form of winds or a low powered jet. In contrast, the powerful jet in M87 is thought to be powered by an accretion disc in the Magnetically Arrested Disc [(MAD), ?] state, wherein accretion on the BH is suppressed by strong poloidal fields. Additional questions include determining whether Sgr A* is disc or jet dominated; the location of the jet base in M87 is in relation to its event horizon; whether the event horizon actually exists; and the orderedness of magnetic fields in the inner accretion disc and jet. (ISCO) spins have been measured for stellar mass black holes

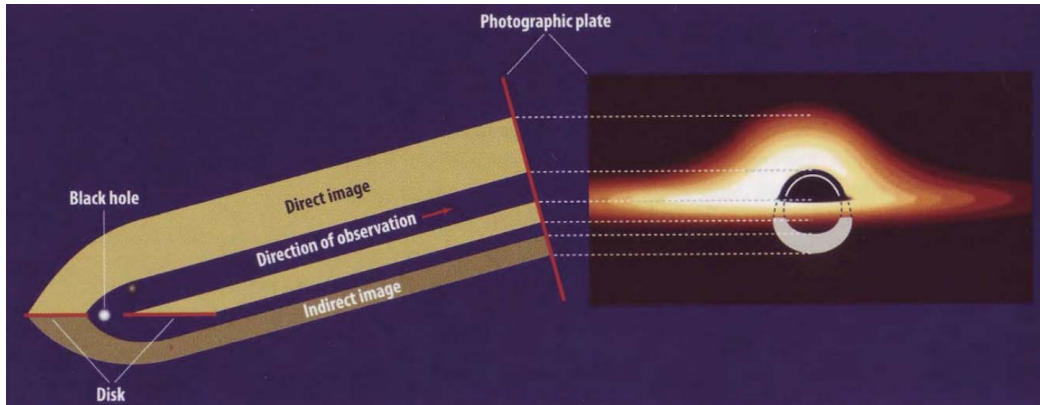


Figure 1.1: (Image credit : Shep Doeleman) Cartoon image (left) combined with the ray-tracing of a thin accretion disc surrounding a BH, first calculated by ?. The cartoon image shows that both the bottom and top of the back of the accretion disc is lensed by the black hole and becomes visible. The dark area in the centre, known as the black hole shadow is the lensed image of the photon ring orbiting the BH. A measurement of its precise shape is a test of general relativity in the strong field regime. Note that the left-right asymmetry in the image is due to doppler boosting, and that all sides of the accretion disk and photon ring are visible due to lensing.

Fortunately, the innermost emission is gravitationally lensed by the SMBH, which causes it to appear magnified by several times its original size. In theory, the innermost orbit should be dominated by a ring of photons, the lensed image of which should feature a shadow-like (or ‘silhouette’) feature [e.g. Johannsen and Psaltis, 2010]. Fig. 1.1 shows an image ray-traced from a General Relativistic Magneto-Hydrodynamic simulation of the accretion disc around Sgr A* [Mościbrodzka et al., 2014]. The circular shadow is apparent in the centre of the image. The two primary targets Sgr A* and M87 are expected to have gravitationally-lensed photon rings with apparent angular diameters of $\theta_{\text{pr}} \sim 50$ and $\sim 20 - 40 \mu\text{-arcsec}$ respectively [Broderick and Loeb, 2009, Falcke and Markoff, 2013], and hence should be resolvable by the EHT.

1.1.2 Measuring space-time in strong gravity

Gravity as described by General Relativity (GR) is consistent with all observational experiments thus far [e.g. ?], however GR has conceptual weaknesses, especially as it is not compatible with the quantum description of reality. Various alternatives to GR have been theorised which do not assume a purely classical description of matter. To compare GR with the alternatives, we have to compare its predictions in the strong, non-linear field regime where the largest deviations from GR would occur if it were an approximate theory.

The spacetime within several R_g around a SMBH provides this opportunity. The precise shape of the photon ring around a SMBH is dependent on the spacetime which in turn is calculated within a theory of gravity [Takahashi, 2004]. The No-Hair theorem, which is based on GR, states that the spacetime should only be determined by the first two moments of the black hole, i.e. its mass and spin. If the No-Hair theorem is invalid, the ring will deviate from a Schwarzschild or Kerr profile. In the case of a non-zero quadrupole moment the ring will become either oblate or prolate [Johannsen and Psaltis, 2010]. This asymmetry is potentially measurable by EHT observations [Broderick et al., 2014].

Is there an event horizon or a surface? - surface would radiate

1.2 Cranking up the angular resolution

Throughout the history of astronomy, there have been celestial sources which appear point-like (unresolved) with the available instrumentation. To investigate the nature of these sources, ever more sophisticated instruments with higher resolution are developed.

In principle, a diffraction-limited aperture can obtain an angular resolution of

$$\theta_{\text{res}} \approx 1.22 \lambda/D, \quad (1.4)$$

where D is the diameter of the aperture and λ is the observing wavelength. However, dish apertures larger than a hundred metres are infeasible to construct while systematic errors, including scattering-induced blurring due to inhomogeneous density (radio) or temperature (optical) distributions in the Earth's atmosphere can lead to instrument being unable to reach the diffraction limit. To overcome these difficulties and improve θ_{res} , a variety of new technologies have been developed (see Fig 1.2), including space-based observatories which escape the limitations set by the Earth's atmosphere, interferometric arrays which eliminate the need to build extremely large apertures, as well as technology-enabled mitigation strategies like adaptive optics and water vapour radiometry which account for atmospheric turbulence in real time.

The observing technique which typically achieves the highest angular resolution is Very Long Baseline Interferometry (VLBI). Interferometry refers to the technique of measuring the electric field correlations (named ‘visibilities’) between pairs of separated antennae. The visibilities are related to Fourier components on a section of approximately flat sky. Through an ‘adequate’ sampling of the Fourier domain an approximate image of sky can be reconstructed using the inverse Fourier transform. With this method, the distance between the antennae (\mathbf{b} , referred to as the ‘baseline’) effectively replaces D in equation 1.4, yielding a higher angular resolution than a single aperture. This technique is primarily used at radio frequencies while the electric field phase remains relatively stable. VLBI is essentially radio interferometry with antennae separated by large distances, typically $\gtrsim 100$ km, including the possibility for antennae in Earth's orbit. A key distinction from connected-element interferometry is that independent clocks are needed at each station to facilitate the post-observation correlation. VLBI has seen several noteworthy achievements since its inception in the late 1960's, including resolution of the extra-galactic, compact, highly-variable objects, now known as quasars into super-luminal core-jet systems [e.g. ?], and the mapping of maser motion around the Super-Massive Black Holes (SMBH) in the cores

of nearby galaxies [e.g. ?].

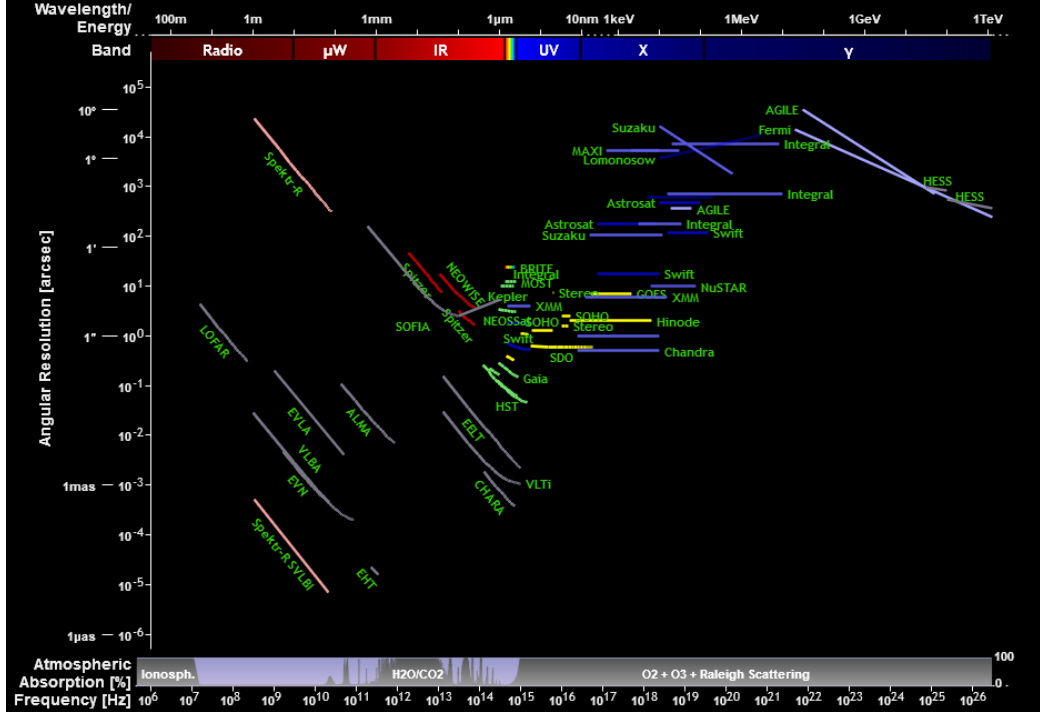


Figure 1.2: (Image credit: Olaf Frohn²) An illustration of angular resolution vs. observing frequency across the entire observational spectrum, shown for a selection of observatories. The VLBI arrays : Spektr-R SVLBI (or RadioAstron) and the EHT clearly achieve the highest angular resolution of all due to their long baselines. At the bottom of the plot, there is a panel showing atmospheric/ionospheric absorption as a function of wavelength, and consequently all observatories in the zero transmission zones are space-based.

As will be described in the next section, the ultra-high angular resolution provided by VLBI enables investigation into several key questions concerning black holes.

1.3 The Event Horizon Telescope

1.3.1 Overview

In the last few decades there has been a push to enhance VLBI capabilities at sub-millimetre wavelengths. One of the leading efforts in this regard is the Event Horizon Telescope consortium [(EHT), Doeleman et al., 2010], an international project whose primary objective is to spatially resolve the lensed photon rings of nearby SMBHs with an angular resolution on the order of their event horizons. In contrast to competing high frequency VLBI observatories e.g. the Very Long Baseline Array (VLBA) which has coverage to 87 GHz (3 mm), the EHT is operating at 230 GHz (1.3 mm) and will potentially extend till 345 GHz (0.8 mm) in the future. See Fig. 1.3 for an annotated map of the locations of the EHT array. As the EHT will have baseline lengths comparable to the diameter of the earth, $|b| \sim 10^4$ km and is operating at 1.3 mm, this yields $\theta_{\text{res}} \sim 30 \mu\text{-arcsec}$ i.e. on the order of θ_{pr} .

Instrumentation and observational challenges

The development of mm-VLBI instrumentation has been spurred by the formation of EHT as a project and the deepening of theory and simulation work over the past two decades. This is evidenced by the comparable observational results but starkly different interpretations of Krichbaum et al. [1998] and Doeleman et al. [2008]. A decade apart, both teams observed Sgr A* with a mm-VLBI arrays consisting of three stations at similar frequency (215 GHz in 1998 and 230 GHz in 2008). Although the former was limited by calibration uncertainties, the primary difference in analysis and interpretation was that the latter result was linked explicitly to the innermost accretion physics in the event horizon region [e.g. Broderick et al., 2011]. In this way, the newly developed theoretical context contributed to the significance of the Doeleman et al. [2008] result. However, to robust comparison with this diverse body of theoretical work would require a significant leap in mm-VLBI observational

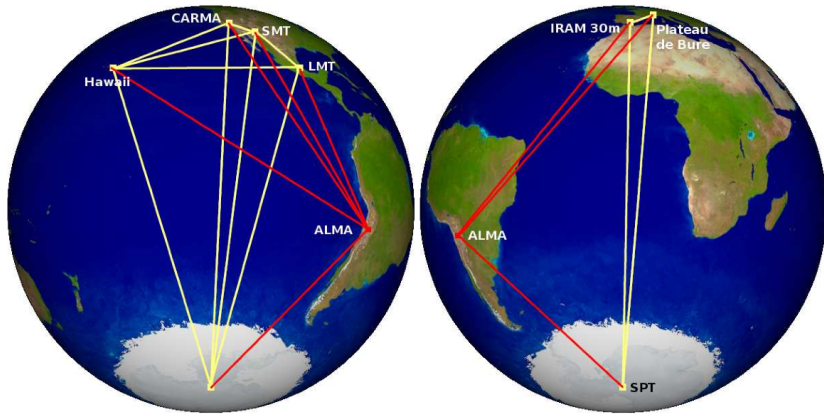


Figure 1.3: (Image credit: Remo Tilanus) The view of the Event Horizon Telescope (EHT) from Sgr A*. This interferometric array uses Earth-diameter baselines, operating at 230–345 GHz to attain an angular resolution of the order of $\theta_{\text{res}} \sim 10 \mu\text{-arcsec}$. Baselines to ALMA are shown in red, to highlight its order of magnitude higher sensitivity. Note that the CARMA station has recently been decommissioned, a telescope in Greenland is currently being constructed and there is ongoing investigation into a possible site on the African continent.

capabilities. For example, to discern whether the No-Hair theorem is violated requires the fractional asymmetry of the shadow shape with respect to its angular size to be measured to a few percent [e.g. Goddi et al., 2016, and references therein]. To achieve this level of precision, the development of the global mm-VLBI array will surely be faces significant challenges.

The move to higher frequencies is accompanied by requirements on the instrument including: increased data rates ($1 \rightarrow 16$ GHz) and stability of timing standards; as well as increased accuracy of dish surfaces and antenna pointing accuracy. Difficulties emerge also from the effects of the Earth's lower atmosphere where optical depth becomes significant and turbulence causes rapid fluctuations in the signal transmission time which causes decoherence in the visibilities. Even though the stations are at high altitude, desert locations, the atmospheric coherence times are still short, typically $\lesssim 10$ s [Doeleman et al., 2009]. The extensive requirements on instruments and location drive up the cost of mm-VLBI stations, resulting in few element (< 10) interferometric arrays which make for sparse sampling of the Fourier domain. This is exacerbated by short mutual visibility windows and imperfect weather. Traditional phase referencing calibration is ruled out due to the variable atmosphere, the lower calibrator source density of the high frequency sky and that calibrators are resolved and variable too at this high angular resolution.

Aside from the considerations listed above, there is a string of complications relating to the target sources, the ISM and the calibration procedure. Firstly, as mentioned earlier, the emission from the primary source Sgr A* is strongly scattered by turbulent electron plasma in the ISM along this line-of-sight. This medium both blurs and introduces random, time-variable substructure into the source brightness distribution (see section 2.2.2). The scattering substructure adds complications for data interpretation as its contribution is difficult to disentangle from that of the intrinsic source substructure, depending on the time-scale of the observation. The second issue is that the source is intrinsically variable over minutes to hours (see section 2.1.4).

The fact that the source is variable over the course of a single observation epoch breaks a fundamental assumption in interferometry as the visibilities cannot be related to a static sky image. This (broken) assumption is central to technique of self-calibration (see section 2.1.2), while in fact both the source and the ISM are time-variable.

These effects, among others, may place significant limitations on the sensitivity, image fidelity, and dynamic range that can be achieved with mm-VLBI observations [Blecher et al., 2016]. Furthermore, unaccounted for systematic and/or non-Gaussian uncertainties could preclude robust, accurate Bayesian parameter estimation and model selection analyses of accretion flow [e.g. Broderick et al., 2016] and gravitational physics [e.g. Broderick et al., 2014, Psaltis et al., 2016], two of the EHT’s many objectives. It is therefore imperative that a deep, quantified understanding of mm-VLBI’s ability to measure and discern between theoretical predictions in the presence of a myriad of signal corruptions.

1.4 A realistic mm-VLBI simulator

Given the significant observational challenges that the EHT faces, we have undertaken this project to build a mm-VLBI observation and signal corruption simulator. There are many benefits for using such a toolkit and indeed synthetic data simulation is common practice for major scientific experiments. A prominent example is the extensive gravitational wave template matching scheme for The Laser Interferometer Gravitational-Wave Observatory (LIGO) which operates in the presence of tidal loading, passing trains etc. In essence such a simulator would fill in the final component of the theoretical signal propagation chain, effectively taking astrophysical simulations of the source (e.g. accretion onto a SMBH) as an input and returning realistic synthetic interferometric data. This allows a more effective interplay between theory and observation, quantifying systematic effects and the

measurement limits. The remainder of this section will briefly discuss several research questions relevant to an EHT synthetic data simulator and how we approach the software design in order to address these questions.

A key use case for simulated data is the testing of calibration, parameter estimation and imaging algorithms and strategies. As the inputs to the simulator are known exactly, we are better able to explore sources of error which are difficult to disentangle from intrinsic source features when using only real data. A straightforward way to perform such a test is through the creation of a set of ‘standard challenge’ dataset. Such datasets would be available to the entire community to input into their calibration and/or imaging routines. Following this, a detailed comparison between the different strategies in varying regimes (source, ISM, troposphere and instrumental) can be made. Importantly, a systematic investigation of a particular algorithm across many different datasets could provide insight into subtle or previously unknowns sources of error inherent in that routine.

Simulated data can also assist in the optimisation of the experimental configuration. Financial constraints require the prioritisation of hardware upgrades e.g. increasing bandwidth, surface accuracy improvement, deployment of water vapour radiometers or additional receiver bands. Simulated data together with calibration and imaging pipelines can help to quantify the benefit of each improvement based on expected scientific return in units of precision of the scientific parameter of interest (e.g. shadow assymetry) rather than more generic terms (e.g. angular resolution, positional uncertainty) that may not have an associated systematic effect included. This approach can even be extended to assess new candidate stations, especially as new geographic locations (e.g. in Southern Africa) are receiving increasing attention due to the potential long baselines to ALMA, SPT and European stations.

Recently, there has been an increase in the attention given to simulating EHT observations of Sgr A* and M87 [Fish et al., 2014, Lu et al., 2014, Bouman et al., 2015, Lu et al., 2016, Chael et al., 2016]. However, these

are primarily focused on image reconstruction and assume either negligible or Gaussian distributed gain errors; perfect antenna pointing accuracy; and in most cases only Gaussian convolution to simulate ISM scattering [Blecher et al., 2016]. Clearly, as the EHT array is enhanced (and possibly expanded), so too must the interferometric simulations evolve to provide ever-more physical predictions on the confidence levels with which parameters can be extracted and hence exclude theoretical models of gravity and/or accretion flows.

Over the past decade, significant effort has been placed on advanced radio interferometric calibration and imaging algorithms for centimetre and metre-wave facilities in response to the large number of new arrays in construction or design phase (e.g. MeerKAT, ASKAP, SKA, LOFAR, HERA). A leading software package in this pursuit is MEQTREES³ [Noordam and Smirnov, 2010], which was developed to simulate, understand and address the calibration issues to be faced with the greatly enhanced sensitivity, instantaneous bandwidth, and field-of-view of such facilities. For example, MEQTREES is rooted in the Measurement Equation mathematical formalism [Hamaker et al., 1996], which parameterizes the signal path into distinct 2×2 complex matrices called Jones matrices. This formalism and applications thereof are laid out in [Smirnov, 2011a,b,c] and are arbitrarily generalized to model any (linear) effect, including undesired signal corruptions that often may have subtle yet systematic effects. MEQTREES has been applied to correct for direction-dependent calibration errors to Karl. G. Jansky Very Large Array (VLA) and Westerbork Synthesis Radio Telescope (WSRT) observations, achieving record-breaking high dynamic range images [Smirnov, 2011c, Makhathini et al, in prep.]. The effectiveness provided by the Measurement Equation formalism in radio interferometric calibration provides a strong motivation to explore its application to the challenging goal of imaging a supermassive black hole silhouette with mm-VLBI. To construct this simulator

³<https://ska-sa.github.io/meqtrees/>

we leverage off metre and cm-wavelength simulation and calibration successes and build a MEQTREES-based mm-VLBI-specific software package which we name, MEQSILHOUETTE. Use of MEQTREES and MEASUREMENT SET data format lends itself to investigating a range of different techniques that are used in other areas of interferometry [e.g. ?]. While MEQTREES has not yet been used in the context of mm-wavelength observations, the framework is agnostic to higher frequency implementation as long as the Measurement Equation is appropriately constructed.

1.5 Outline

This thesis is broadly divided into the following chapters and sections,

- **Chapter 2 : Theory**

Section 2.1 introduces radio interferometry via the Measurement Equation formalism, followed by mm-VLBI tailored discussions on calibration, data products and the consequences of breaking the static source assumption.

Section 2.2 is a review and investigation into the key signal corruptions implemented in the MEQSILHOUETTE simulator i.e. instrumentation imperfections and transmission through the ISM and Earth's atmosphere.

- **Chapter 3 : Software Implementation**

Section 3.1 summarises the key software design objectives considered.

Section 3.2 is a description of the design and construction of the simulation software with emphasis on the software architecture and workflow.

- **Chapter 4 : Results and Analysis**

Section 4.1 showcases the basics of the simulator output through a series of canonical results.

Section 4.2 presents a more sophisticated scenario which tests an AIPS calibration routine in the presence of source and tropospheric time-variability.

- **Chapter 5 : Conclusions and future work**

We summarise the work and context of this thesis as well as make suggestions for future applications and improvements.

Chapter 2

Theory

In this chapter we review and develop the theory required to model signal transmission from cosmic source to uncalibrated (raw) interferometric data. The first half of this chapter provides the necessary introduction to fundamental radio interferometric concepts while the second half is focused specifically on describing several key signal corruptions, relevant to mm-VLBI observations.

2.1 Radio Interferometry

This section is structured as follows: first radio interferometry is introduced using the Radio Interferometric Measurement Equation (RIME) formalism, which serves as a guiding framework for the construction of the MEQSIL-HOUETTE simulator. We then review the technique of self-calibration, typical mm-VLBI data products and the consequences of breaking the static source assumption.

2.1.1 Measurement Equation

The RIME provides the notation and formalism to model the signal transmission path as a sequence of linear operations. It takes into account polarisa-

tion, correlation and the correct time-ordering of signal transmission path in an intuitive and efficient way. The formalism also enables a more informative phrasing of the relation between calibration and signal corruptions.

Here we offer a short derivation and explanation of the RIME following Smirnov [2011a]. Consider a quasi-monochromatic, complex-valued electric field vector \mathbf{E} , which can be decomposed into an arbitrary two dimensional orthogonal basis in the plane perpendicular to the direction of propagation,

$$\mathbf{E} = \begin{pmatrix} E_a \\ E_b \end{pmatrix},$$

where this choice represents the basis in which the polarisation is measured. All linear transformations of the above electric field can be written by a multiplication with a 2×2 complex valued matrix, termed a *Jones* matrix [?][ads was down!],

$$\mathbf{E}' = \mathbf{J}\mathbf{E}. \quad (2.1)$$

For example, the conversion of the electric field to a voltage \mathbf{v} at an antenna can be specified by such a transformation i.e. $\mathbf{v} \equiv \mathbf{E}'$ under multiplication with the appropriate \mathbf{J} . Multiple effects then can be represented by multiplication of various Jones matrices, forming a Jones chain,

$$\mathbf{E}' = \mathbf{J}_n \dots \mathbf{J}_1 \mathbf{E}. \quad (2.2)$$

The order of the Jones matrices should obey the causal order of the signal transmission path (i.e. \mathbf{J}_1 would closest to source, \mathbf{J}_n closest to antenna). However the rules of commutivity of matrices allows us some flexibility. Matrices which are scalar commute with everything, while diagonal matrices commute with each other as do matrices which effect a rotation of \mathbf{E} . This allows the Jones chain to be re-ordered into more convenient formulations as required. In other words, the signal path can parameterised in different ways. For example during calibration, it is useful to construct a *phenomeno-*

logical Jones matrix which represents the combined action of several *physical* commuting processes/matrices (e.g. ionospheric delay and electronic drift). The advantage would be that only the cumulative effect is considered, which keeps the number of parameters to solve for to a minimum. This would be useful when the individual effects cannot be easily distinguished and/or have the same Jones matrix form. On the other hand, for realistic data simulation, we prefer to model the signal transmission path by formulating a Jones matrix based on the exact physical process.

An interferometer measures the correlation of the voltages from an antenna pair, referred to as a *baseline*. The correlator output is termed the *visibility*,

$$\mathbf{V}_{pq} = \langle \mathbf{v}_p \mathbf{v}_q^H \rangle, \quad (2.3)$$

where p, q are refer to the two antennae. The representation of \mathbf{V}_{pq} as a 2×2 matrix is equivalent to the Stokes polarisation formulation, for example in an XY basis,

$$\mathbf{V}_{pq} = \mathbf{J}_p \langle \mathbf{E}_p \mathbf{E}_q^H \rangle \mathbf{J}_q^H \quad (2.4)$$

$$= \mathbf{J}_p \begin{pmatrix} \langle E_{xp} E_{xq}^* \rangle & \langle E_{xp} E_{yq}^* \rangle \\ \langle E_{yp} E_{xq}^* \rangle & \langle E_{yp} E_{yq}^* \rangle \end{pmatrix} \mathbf{J}_q^H \quad (2.5)$$

$$= \mathbf{J}_p \begin{pmatrix} I + Q & U + iV \\ U - iV & I - Q \end{pmatrix} \mathbf{J}_q^H, \quad (2.6)$$

where I is the coherence of the total flux, V is the coherence of the circularly polarised flux, Q and U relate to coherence of the linear polarisation. Note that the Jones matrices are assumed to be constant over the time and frequency averaging interval. As this formalism is coordinate system independent, we can easily transform any 2×2 from a linear to circular basis and vice-versa.

We now review the RIME for a single, uncorrupted, unpolarised point

source, which will illustrate the Fourier transform relation between the measured visibility and a section of approximately flat sky. Considering that there are no signal corruptions, the only Jones matrix to consider is the effect of the phase difference of the electric fields measured at the two antennae. This is due to the difference in propagation path length.

Consider the unit vector $\hat{\sigma}$ which points from the centre of the Earth towards the source. We define the position difference between the two antenna or baseline vector in a convenient coordinate system as $\mathbf{u} = (u, v, w)$, with the w-axis in the direction of $\hat{\sigma}$ as shown in Fig. 2.1. Next we denote the angular position on the sky by (l, m) which are the directional cosines on the sky measured in the direction of (u, v) respectively. Note that we consider only a small approximately flat section of the celestial sphere centred on $\hat{\sigma}$, also called the *phase centre*. The phase difference between rays arriving at the two antennae is therefore,

$$\delta\phi = 2\pi(\mathbf{u}/\lambda \cdot \hat{\sigma}) \quad (2.7)$$

As we are only interested in a small, approximately planar component of the sky (i.e. $l^2 + m^2 \ll 1$),

$$\delta\phi \approx 2\pi\lambda^{-1}(u_p l + v_p m). \quad (2.8)$$

Denoting the brightness matrix $\mathbf{B} = \langle \mathbf{E}_p \mathbf{E}_q^H \rangle = !!IdentityMatrix!!?I$ and setting the delay of antenna q as the reference, the RIME for our simplified model becomes

$$\mathbf{V}_{pq} = K_p \mathbf{B} K_q^H \quad (2.9)$$

$$= [\exp(2\pi i\lambda^{-1}(ul + vm))] \mathbf{B} [1] \quad (2.10)$$

where K was the Jones matrix used to apply the phase difference to each antenna. This is a Fourier Transform relation between visibility domain (u, v)

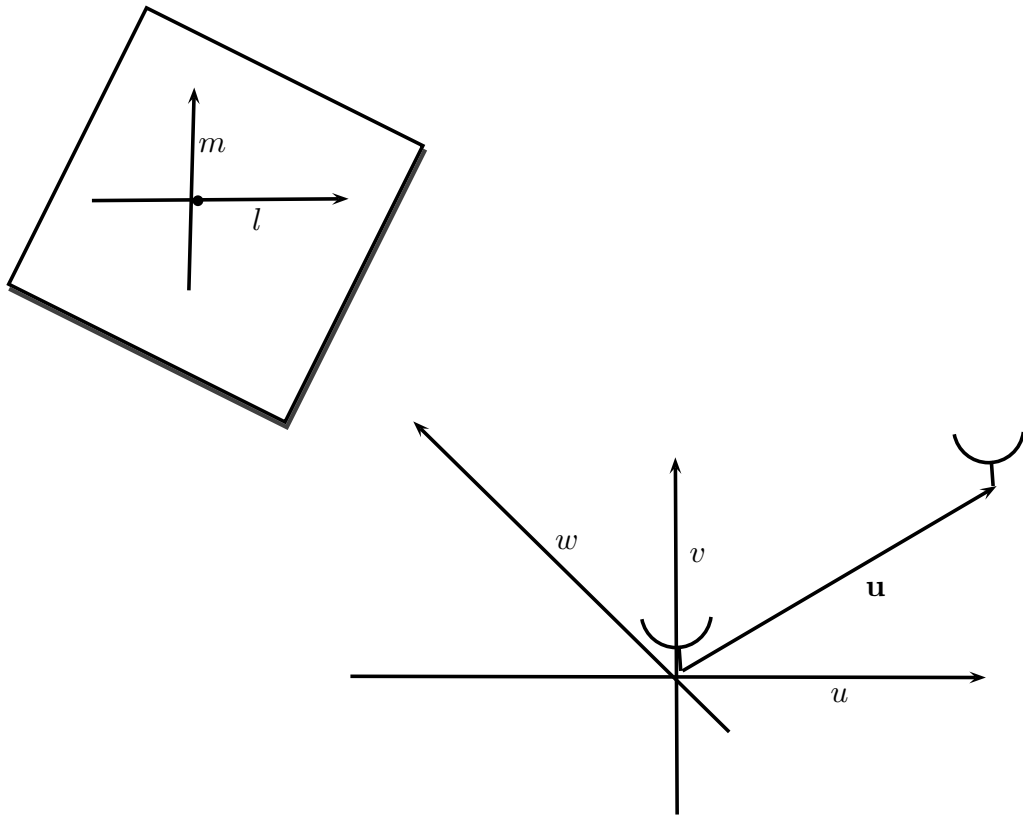


Figure 2.1:

and image domain (l, m) . This derivation can be easily broadened to include extended sources (e.g. see [Smirnov, 2011a]). The quantity $K_p \mathbf{B} K_q^H$ is often denoted as \mathbf{X}_{pq} and is termed the coherency matrix.

An example of a Jones matrix representing a signal corruption is the complex time-variable antenna gain. Considering two independent linear dipoles, for antenna p

$$\mathbf{G}_p(t) = \begin{pmatrix} g_x(t) & 0 \\ 0 & g_y(t) \end{pmatrix} \quad (2.11)$$

Hence the RIME in this case becomes,

$$\mathbf{V}_{pq} = \mathbf{G}_p \mathbf{X}_{pq} \mathbf{G}_q^H. \quad (2.12)$$

2.1.2 Self-calibration and fringe-fitting

We now discuss two (similar) algorithms, self-calibration and fringe-fitting, which are central to VLBI calibration. Our motivation is that we are interested how these algorithms fare in the context of the observational challenges faced by the EHT (see section 1.3.1). Crucially, the MEQSILHOUETTE simulator is able to provide the synthetic datasets on which to run these algorithms, the reconstructions can then be compared to the true signal.

Self-calibration, as the name suggests, uses the target itself as a calibrator to estimate station gains. The algorithm consists of the following iteration: iteratively solve for station gains but not their derivatives whilst constructing the sky model. We begin with the initial sky model (typically a point source) as well as the station gains output by the fringe fit. Then we solve equation 2.12 using a least squares procedure but without taking into account station gain phase derivatives so that there are fewer free parameters. The resulting dataset is then imaged, deconvolved (i.e. the effect of the synthesised beam is removed) and a source finder is applied on the image to construct a more accurate sky model. This sequence is then repeated with the updated sky model being used when solving for station gains. The loop will terminate when a specified flux threshold is reached.

From the point of view of the RIME, fringe-fitting solves for station gains in equation 2.12 over a time interval typically on the order of minutes. Taking a linear expansion in frequency and time of the phase of the station gain yields,

$$\begin{aligned} \mathbf{V}_{pq}(t_0, dt, \nu_0, d\nu) = & |G_p| |G_q| \mathbf{X}_{pq} \exp(i[\phi_p(t_0, \nu_0) + \partial_t \phi_p(t, \nu_0) dt \\ & + \partial_\nu \phi_p(t_0, \nu) d\nu - \phi_q(t_0, \nu_0) - \\ & \partial_q \phi_p(t, \nu_0) dt - \partial_\nu \phi_q(t_0, \nu) d\nu]). \end{aligned} \quad (2.13)$$

The above is normally phrased in terms of time delay and the rate of time delay

The terms $\phi(t_0, \nu_0) + \partial_\nu \phi_p(t_0, \nu) d\nu$ is known as the delay (check)

A blind search (iterate through a range of delay and rate values in a user-specified range, maximising the correlation amplitude) is then performed for all the station based parameters in the above equation i.e. everything except \mathbf{X}_{pq} . The station gain amplitude will sometimes be calibrated separately, reducing the number of parameters to solve. The sky model used is typically just a point source at the centre of the field.

with the observational with a variable source, tropospheric, ISM and instrumental signal corruptions is of central interest to this investigation.

2.1.3 mm-VLBI observables and data products

If the visibility amplitude and phase are highly variable as in the case of a turbulent atmosphere with non-negligible opacity, conventional calibration and imaging techniques have severely limited (if any) success. However, information can still be extracted from the raw visibilities in the form of closure quantities [Monnier, 2007] or polarisation ratios [Fish et al., 2009]. Visibility amplitudes are also used although they suffer from systematic errors, a subset of which are dealt with in this work. Some imaging algorithms use a technique called ‘hybrid mapping’ [e.g. Lu et al., 2014, Bouman et al., 2015, Chael et al., 2016] which use closure phase as a regulariser to ensure that imperfect calibration of station gains do not affect the resulting image, although

these unconventional imaging algorithms come with their own uncertainties on uniqueness and repeatability. Closure phase, defined as the sum of visibility phases of a triangle of stations $\{i, j, k\}$, is a probe of point-asymmetry in source structure,

$$\Phi_{ijk} = \phi_{ij} + \phi_{jk} + \phi_{ki}. \quad (2.14)$$

Because many of the dominant signal corruptions are station-based, the gain phase terms $\phi_{ij} = \phi^{\text{true}} + \phi_i^G - \phi_j^G$ for each antenna, assuming they are constant over the integration time and bandwidth, will cancel which yields a more robust observable. In the literature, the uncertainty on the closure phase is calculated in various ways. One method is model dependent [Rogers et al., 1995] and is given as a function of the SNR s of each baseline

$$u(\Phi_{ijk}) = \frac{\sqrt{4 + (s_{ij}s_{jk})^2 + (s_{jk}s_{ki})^2 + (s_{ij}s_{ki})^2 + 2(s_{ij}^2 + s_{jk}^2 + s_{ki}^2)}}{s_{ij}s_{jk}s_{ki}}, \quad (2.15)$$

where s_{ij} is defined as

$$s_{ij} = |V_{ij}| \sqrt{\frac{\tau \Delta \nu}{SEFD_i SEFD_j}}, \quad (2.16)$$

where τ is the vector averaging timescale, $\Delta \nu$ is the bandwidth, $|V_{ij}|$ is the visibility amplitude of the assumed source model and $SEFD$ is the system equivalent flux density.

Alternatively, assuming Gaussian errors the uncertainty on the closure phase over a scan $u(\Phi_{ijk}) = \sigma(\Phi_{ijk})/\sqrt{n}$ [Brinkerink et al., 2016].

2.1.4 Variability and the static source assumption

Implicit in our description of interferometry above (e.g. equation 2.9), we assumed that the source remains approximately unchanged or static during the course of the observation. However, if this assumption does not hold (i.e.

if the source is time-variable), the visibilities measured over the course of an observation can no longer be related to a single image. Note that I am using the term ‘variability’ in a general sense which refers to changes in any source observables. Variability is most often used to denote changes in source flux but we extend the definition to include changes in source structure, position and polarisation. We expect that an image of a variable source would appear smeared out as it is averaged over many realisations and that ghosts should arise during the calibration/deconvolution procedure [**citations? trienko’s papers?**] . One of the objectives of this thesis will be to characterise the errors which emerge when a variable source is self-calibrated in the presence of tropospheric-induced errors. Practically it is difficult to separate source and instrumental variability without accurate models for both.

Although the static source assumption holds for most interferometric observations, the accretion flow and/or magnetic field structures around a SMBH can be variable on far shorter timescales. The primary mm-VLBI target, Sgr A*, exhibits variability on timescales of minutes to hours in the high frequency radio (including EHT observations), near-infrared (NIR), and X-ray bands [e.g. Baganoff et al., 2001, Genzel et al., 2003, Yusef-Zadeh et al., 2006, ?, Fish et al., 2011, Johnson et al., 2015]. This wealth of observational data has yielded several constraints but the origin of the variability is still highly debated.

To explain the observed delays between flares in different frequency bands, an expanding adiabatic plasma model [e.g. Marrone et al., 2008][!not sure on ads] has been presented, however a recent flare observed with the EHT did not exhibit the increase in size expected from an expanding plasma outflow model Fish et al. [2011]. Signatures of periodic variability at NIR and X-ray [Genzel et al., 2003, Bélanger et al., 2006] have been used to argue for the presence of orbiting hotspots Doeleman et al. [2009]. As the Innermost Stable Circular Orbit (ISCO) depends on spin of the BH, the spin can be constrained through the detection periodic orbital features. On the other

hand, a more recent observation of a longer light curve in the NIR is more representative of a power-law scale variability Meyer et al. [2008]. The cumulative evidence of these observations point to the possibility of multiple flaring mechanisms. An important mm-VLBI observational result is that variability in the polarisation domain is far more rapid than the total intensity (Johnson 2015b), indicating that the magnetic fields structure is highly dynamic.

In principle, the variability timescale could be comparable to the period of the Innermost Stable Circular Orbit (ISCO), which for Sgr A*, ranges from 4 minutes in the case of a maximally rotating BH with a prograde disc to about half an hour for a non-rotating BH. The ISCO period for M87 is substantially longer, on the order of days [refs]. Considering light crossing times Δt_{cross} , we can estimate the angular size θ of the emission region to be of order $\theta \sim \Delta t_{\text{cross}} c / D_{\text{src}}$, where c is the speed of light and D_{src} is the observer-source distance. Hence for Sgr A* at $D_{\text{src}} = 8.3$ kpc (Gillessen, 2009), a flare of duration $\Delta t_{\text{cross}} = 10$ min corresponds to scales of $15 R_{\text{Sch}}$. Such analyses gave early evidence for an emission area on event horizon scales.

In the case of a highly localised flare, several approaches [Doeleman et al., 2009, ?, Johnson et al., 2014] show that EHT can track such a structure with ~ 5 μ -arcsec precision using closure quantities and polarimetric ratios, assuming that ALMA is participating in the array. This could help map the space-time around the BH. Alternatively Lu et al. [2016] show that a Gaussian weighting scheme can be applied to mitigate the effects of variability and measure the quiescent structure although this approach would down-weight the longest baselines. However all of these approaches assume only Gaussian thermal noise, Gaussian-blurring in the ISM and no tropospheric-induced calibration errors.

2.2 Signal Corruptions

In this chapter we explore in detail signal corruptions due to the transmission through the ISM and Earth’s atmosphere as well as instrumental imperfections, in order for these corruptions to be implemented in the MEQSILHOUETTE simulator.

2.2.1 Scattering basics

Millimetre wavelength radiation originating at the Galactic Centre is repeatedly scattered along the signal path to the Earth-based observer. The first occurrence is due to electron plasma in the ISM [e.g. Bower et al., 2006, Gwinn et al., 2014], while the second is due to poorly-mixed water vapour in the Earth’s troposphere [e.g. Lay, 1997, Carilli and Holdaway, 1999]. It is essential that the effects of the scattering phenomena are understood for accurate calibration and robust inference of the intrinsic source properties. As an introduction to the separate descriptions of each, we review a simple scattering model.

An electro-magnetic wave is scattered when it passes through a medium with refractive index inhomogeneities. Following Narayan [1992], this effect can be modelled as a thin screen, located between source and observer planes and orientated perpendicular to the line-of-sight. The screen, with 2D coordinates \mathbf{x} , adds a stochastic phase $\phi(\mathbf{x})$ to the incoming wave at each point on the screen, yielding a corrugated, outgoing wavefront. We define the Fresnel scale as $r_F = \sqrt{\lambda D_{os}/2\pi}$, where D_{os} is the observer-scatterer distance. r_F represents the distance where the geometrical path difference $\frac{2\pi}{\lambda}(D_{os} - \sqrt{D_{os}^2 + r_F^2}) = \frac{1}{2}$ rad.

To determine the resultant electric field at a point in the plane of the observer, indexed by coordinate vector \mathbf{X} , one has to take into account all possible ray paths from the screen to \mathbf{X} . To illustrate the model, a calculation of the scalar electric field generated by a point source, $\psi(\mathbf{X})$

yields the Fresnel-Kirchoff integral [Born and Wolf, 1980]

$$\psi(\mathbf{X}) = C \int_{\text{screen}} \exp \left[i\phi(\mathbf{x}) + i \frac{(\mathbf{x} - \mathbf{X})^2}{2r_F} \right] d\mathbf{x}, \quad (2.17)$$

where C is a numerical constant.

The statistical properties of $\phi(\mathbf{x})$ can be described by a power spectrum or equivalently the phase structure function,

$$D_\phi(\mathbf{x}, \mathbf{x}') = \langle [\phi(\mathbf{x} + \mathbf{x}') - \phi(\mathbf{x})]^2 \rangle, \quad (2.18)$$

where \mathbf{x} and \mathbf{x}' represent two points on the screen and $\langle \dots \rangle$ denotes the ensemble average.

There is evidence that D_ϕ can be reasonably approximated by a power law dependence on the absolute distance r between points on the screen [Armstrong et al., 1995, ?]

$$D_\phi(r) = (r/r_0)^\beta, \quad r^2 = (\mathbf{x} - \mathbf{x}')^2 \quad (2.19)$$

where r_0 is the phase coherence length scale defined such that $D_\phi(r_0) = 1$ rad. Kolmogorov turbulence, which describes how kinetic energy injected at an outer length scale r_{out} cascades to increasingly smaller scales until finally dissipated at an inner length scale r_{in} , predicts $\beta = 5/3$ in the domain $r_{\text{in}} << r << r_{\text{out}}$. This scaling has been demonstrated to be a reasonable approximation for the ISM over scales $r \sim 10^2$ km to > 1 AU [Johnson and Gwinn, 2015], and also for the troposphere with $r < \Delta h$, where Δh is the thickness of the turbulent layer Coulman [1985]. The specifics of the tropospheric model will be explored further in later sections.

The two length scales, r_F and r_0 , define the nature of the scattering which is split into the strong and weak regimes, Fig. 2.2. In weak scattering, $r_0 \gg r_F$ and hence by equation 2.19, $D_\phi(r_F) \ll 1$. This implies that most of the radiative power measured on a point \mathbf{X} will originate from a screen area

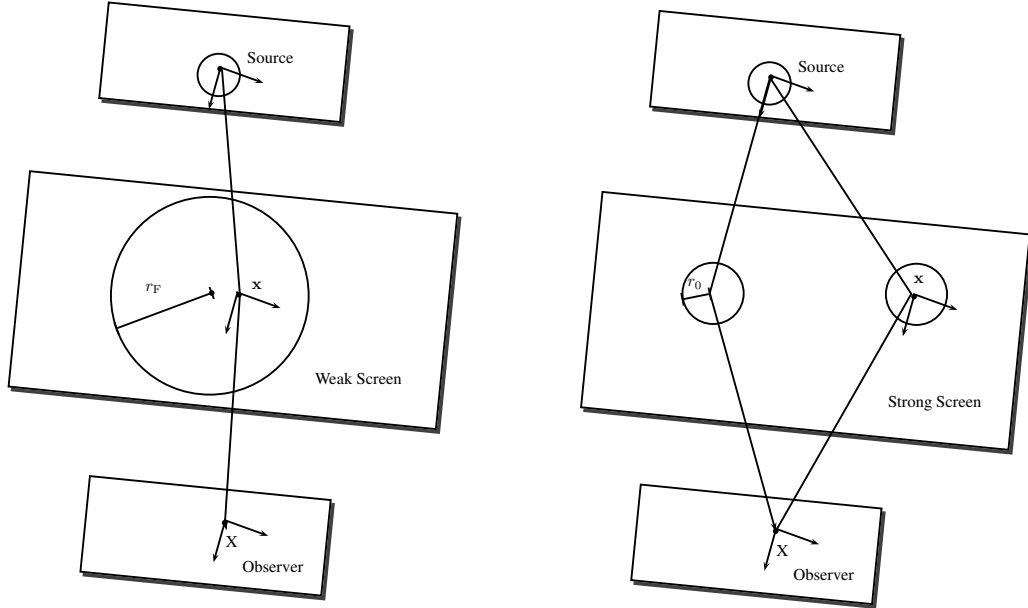


Figure 2.2: Illustration depicting the basics of scattering in the weak (left) and strong (right) regimes. In the weak regime, the signal is coherently propagated over an area, $A_{\text{weak}} \approx \pi r_F^2$, whereas in the strong regime, coherent propagation is split over many areas, each of size $A_{\text{strong}} \approx \pi r_0^2$.

$A_{\text{weak}} \approx \pi r_F^2$. Whereas in the regime of *strong scattering*, $r_0 \ll r_F$ yielding $D_\phi(r_F) \gg 1$. This results in coherent signal propagation onto the point \mathbf{X} from multiple disconnected zones each of area $A_{\text{strong}} \approx \pi r_0^2$ [Narayan, 1992]. Scattering in the troposphere and ISM in the direction of the Galactic Centre fall into the regimes of weak and strong scattering respectively.

To evolve the screen in time, we assume a frozen screen i.e. that the velocity of the individual turbulent eddies is dominated by the bulk motion of scattering medium [e.g. Lay, 1997]. This allows us to treat the screen as frozen but advected over the observer by a constant motion. Hence time variability can be easily incorporated by the relative motion between source, scattering screen and observer.

2.2.2 Interstellar medium scattering

Electron density inhomogeneities in the interstellar medium (ISM) plasma scatter the radio emission from the Galactic Centre. Radio interferometric observations of Sgr A* have characterised the basic properties of the intervening plasma material, however extensive developments in scattering theory and simulations have proved essential to the interpretation of more subtle scattering phenomena. This section begins with the earlier, longer wavelength VLBI results which studied the Gaussian blurring effect of the scattering of SgrA*; we then expand on the scattering theory introduced in Sec. 2.2.1 to review the latest theoretical developments which explore the presence of scattering-induced substructure; finally we review recent observational results which account for scattering substructure in their data interpretation.

The dominant observational effect of this scattering scenario for $\lambda \gtrsim 1$ cm is to convolve the intrinsic source structure with an elliptical Gaussian. The size of the Guassian exhibits a λ^2 scaling dependence over several orders of magnitude [Fig. 2.3 ?Shen et al., 2005, Bower et al., 2006, Lu et al., 2011], which is consistent with the wavelength dependence of the refractive index of a plasma. In order to determine the parameters of the scattering kernel, i.e. major axis, minor axis and position angle, one has to observe at wavelengths where the angular size of scattering ellipse is much larger than the expected source size. A Very Long Baseline Array (VLBA) + Green Bank Telescope (GBT) campaign Bower et al. [2006] estimated the size at 1.31×0.64 mas cm $^{-2}$, oriented 78° east of north.

An accurate extrapolation of scattering kernel to 1.3 mm is important for the EHT scattering-mitigation strategy Fish et al. [2014] which aims to deblur the scattered image through a deconvolution procedure. However as this extrapolation is over at least an order of magnitude, any small systematic error in the original measurement can significantly effect the 1.3 mm extrapolated parameters. A recent review of VLBI observations of Sgr A* Psaltis et al. [2015] has noted that there are significant inconsistencies be-

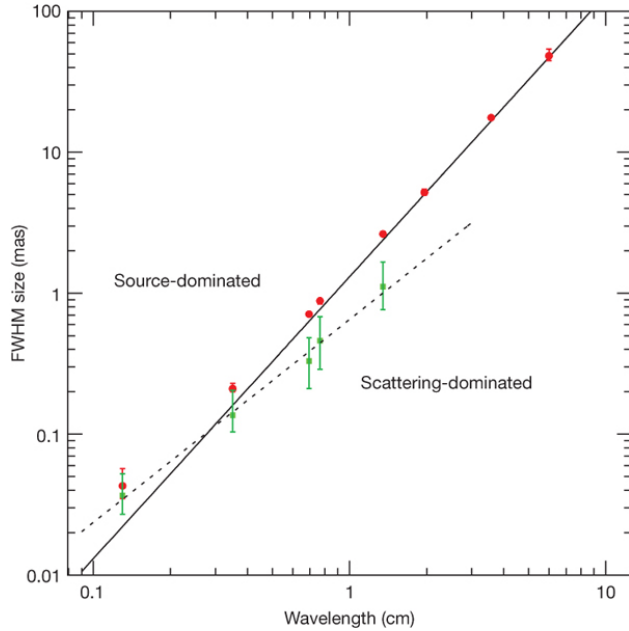


Figure 2.3: The λ^2 dependence of scattering kernel size is shown by the solid line. This has been derived from measurements made at $\lambda > 17$ cm Bower et al. [2006]. The dotted line shows the derived intrinsic source size which scales as $\lambda^{1.44}$. This was derived from measurements in the wavelength range, $2\text{ cm} < \lambda < 1.3\text{ mm}$ [Doeleman et al., 2008]. The red circles show major-axis observed sizes of Sgr A* and the green points show the derived intrinsic major-axis size. This plot was reproduced from Doeleman et al. [2008].

tween different measurements. The authors used a Bayesian methodology to re-analyse the datasets resulting in increased uncertainties as shown in table 2.1. The minor axis has a much larger uncertainty than the major axis due to the limited north-south coverage of the VLBA array.

The Gaussian blurring effect can explained by the simple scattering model introduced in Sec. 2.2.1. Recall, that in the strong scattering regime light is propagated from coherent patches with linear size $\sim r_0$. Each patch will emit light coherently into a single-slit diffraction cone of angular size $\theta_{\text{scatt}} \sim \lambda/r_0$. An observer will hence be illuminated by many patches spanning θ_{scatt} ,

Table 2.1: A re-analysis of VLBI observations of Sgr A* by Psaltis et al. [2015] has yielded revised estimates of the parameters associated with the Gaussian scattering kernel. Note that the position angle is measured East of North.

major axis FWHM (mas/cm ⁻²)	1.32	0.04
minor axis FWHM (mas/cm ⁻²)	0.82	0.21
position angle (°)	77.8	9.7

yielding a blurred and broadened image, with projected size on the screen equal to the *refractive scale*

$$r_{\text{ref}} = \theta_{\text{scatt}} D_{\text{os}} = r_F^2 / r_0.$$

r_{ref} is the third fundamental length scale in the strong scattering regime and is associated with the refractive timescale,

$$t_{\text{ref}} = r_{\text{ref}} / v.$$

We can calculate r_0 given the FWHM of θ_{scatt} through the more precise relation

$$\theta_{\text{scatt}} = \frac{2\sqrt{2 \ln 2}}{2\pi} \lambda / r_0 (M + 1) \quad (2.20)$$

where $M = D_{\text{os}} / R$ is the magnification and R is the source-screen distance. The magnification factor is a correction to the model introduced in Sec. 2.2.1 when $R \approx \infty$ no longer holds and should be used when calculating distances in the observer plane [Goodman and Narayan, 1989]. The location of the scattering medium was originally thought to be quite close to Sgr A*. However, observations of a newly discovered pulsar, SGR J1745-29, indicate that the scattering screen is located at a distance $D_{\text{os}} = 5.8 \pm 0.3$ kpc, within the Scutum spiral arm. Using Eq. 2.20 and the parameters given in table 2.1, we find that the major axis of the coherence length at 1.3 mm, $r_0 \approx 3136.67$ km.

As the VLBI moves to higher frequencies, focus has shifted away from the well-studied Gaussian convolution effect of ISM scattering and onto the

presence of stochastic scattering-induced substructure. To understand this phenomenon, we must first develop the theory to be sensitivity to the averaging effects of the observation.

Strong scattering can be further subdivided into *snapshot*, *average* and *ensemble-average* regimes [Narayan and Goodman, 1989, Goodman and Narayan, 1989]. To understand the different regimes, remember that for each point on the source, the observer sees emission from coherent patches of area $\sim \pi r_0^2$ over an area $\sim \pi r_{\text{ref}}^2$. The diffraction cones from each of the patches will interfere, resulting in a multi-slit *diffractive scintillation* pattern.

In the *snapshot regime*, a compact source is observed with a narrow bandwidth and over a short time integration. This yields a single realisation of the diffractive scintillation pattern. By averaging over many snapshots, diffractive scintillation is quenched. This occurs if the source size θ_{src} is much larger than the diffractive scale $\theta_{\text{src}} \gg r_0/D_{\text{os}}$; if the fractional bandwidth $\delta\nu/\nu$ is much larger than the decorrelation bandwidth $\delta\nu/\nu \gg \delta\nu_{\text{dc}}/\nu \approx (r_0/r_F)^2$ [Narayan, 1992]; or if the integration time t_{int} is much larger the diffractive timescale $t_{\text{int}} \gg t_0 = r_0/v$, where v is the relative velocity between screen, source and observer. This regime is hence only accessible through observations of compact objects like pulsars. On a side note, observations in this regime can be used to probe the source with angular resolution $\sim \lambda/r_{\text{ref}}$ [e.g. Gwinn et al., 2012]. This is because the scattering screen is essentially a lens of diameter $\approx r_{\text{ref}}$.

In the *average regime*, diffractive scintillation has been averaged over, however there still exists scintillation over scales comparable to the size of the scattered image of a point source $\sim r_{\text{ref}}$, termed *refractive scintillation*. Phase fluctuations on this scale acts like a weak lens to focus or defocus the λ/r_0 scale diffraction cones in the direction of the observer. For a point source this would lead to weak flux variations in the total flux [Narayan, 1992]. We will show later that refractive scintillation leads to the presence of substructure for a resolved scatter-broadened source. In contrast to diffractive scintillation, refractive scintillation is much more difficult to average

over. Typically the refractive time scale $t_{\text{ref}} = r_{\text{ref}}/v$ is on the order of weeks to months for scattering towards the Galactic Centre; the fractional decorrelation bandwidth is on the order of unity $\delta\nu_{\text{dc}}/\nu \sim 1$; and the source has to be much larger than the image of a scattered point source $\theta_{\text{src}} \gg \theta_{\text{scatt}}$.

In the *ensemble-average regime*, both diffractive and refractive scintillation have been averaged over. It is in this regime when the scattering is equivalent to Gaussian convolution which is deterministic and not time variable.

A recent theoretical work [Johnson and Gwinn, 2015] has derived a useful approximation of the resolved scattered image I_{ss} in the average regime,

$$I_{\text{ss}}(\mathbf{x}) \approx I_{\text{src}}(\mathbf{x} + r_{\text{F}}^2 \nabla \phi(\mathbf{x})), \quad (2.21)$$

where ∇ is the directional derivative. Here we have used the same two-dimensional coordinate system, indexed by \mathbf{x} to describe the source, screen and observer planes which are considered to be aligned along the vertical axis. The scattered image I_{ss} is approximated by a ‘reshuffling’ of the source image I_{src} . As $|\nabla \phi| \sim 1/r_0$, the magnitude of the translation of points on $I_{\text{src}} \sim r_{\text{ref}} \sim 10 \mu\text{-arcsec}$ in the case of Sgr A*.

Even though $\phi(\mathbf{x})$ is only coherent to $\sim r_0$, $\nabla \phi(\mathbf{x})$ remains spatially coherent over much larger scales. The autocovariance of phase derivative can be related to the structure function [Johnson and Gwinn, 2015]

$$\langle [\partial_x \phi(\mathbf{x}_0)][\partial_x \phi(\mathbf{x}_0 + \mathbf{x})] \rangle = \partial_x^2 D_\phi(\mathbf{x}). \quad (2.22)$$

A generalised structure function [Tatarskii, 1971, Narayan and Goodman, 1989] is quadratic (r^2) at small scales ($r \ll r_{\text{in}}$), Kolmogorov in the range $r_{\text{in}} < r < r_{\text{out}}$ and constant for $r > r_{\text{out}}$. Taking the simplifying case of $r_{\text{in}} \gg r_0$ and $r_{\text{in}} < r < r_{\text{out}}$ D_ϕ becomes[?],

$$D_\phi = \frac{2}{\beta} \left(\frac{r_{\text{in}}}{r_0} \right)^{2-\beta} \left(\frac{r}{r_0} \right)^\beta \quad (2.23)$$

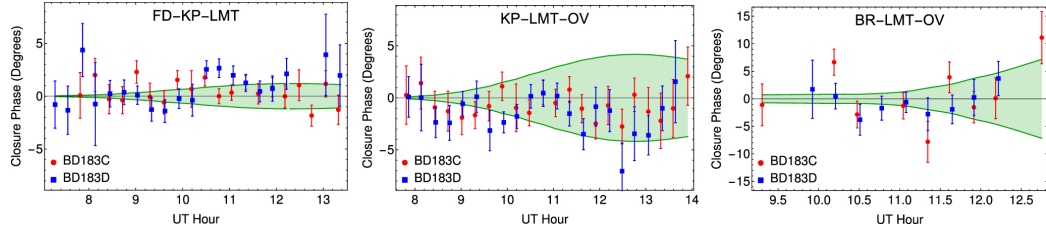


Figure 2.4: Closure phases recorded in a VLBA + LMT observation of Sgr A* at $\lambda = 3.5$ mm ?. The data points are shown as red circles and blue squares and are only distinguished by the calibrator used. The green envelopes show the 1σ closure phase prediction induced by scattering-induced substructure. Reproduced from ?.

Hence, $\partial_r^2 D_\phi(\mathbf{r}) \propto r^{\beta-2}$. Therefore in the Kolmogorov regime ($\beta = 5/3$), the coherence of image shift relative to the refractive scale $\propto (r/r_0)^{-1/3}$. Note that a large inner scale extends coherence of $\nabla\phi$, whereas as $r \rightarrow r_{\text{out}}$ the coherence falls quickly. Therefore, even though $\phi(\mathbf{x})$ is only coherent to $\sim r_0$, $\nabla\phi(\mathbf{x})$ remains spatially coherent over much larger scales, leading to the presence of refractive substructure [Johnson and Gwinn, 2015].

A recent observation of Sgr A* at 3.5 mm by the VLBA+LMT [see Fig. reffig:substructure2 ?] has measured non-zero closure phases on its longest baselines. However it was also shown in the data analysis that the measured values are consistent with expectation refractive scintillation assuming a circular Gaussian source of FWHM = 130 $\mu\text{-arcsec}$. Another observation at 1.3 cm shows flux modulation due to scattering substructure ~ 10 mJy [Gwinn et al., 2014] and other predictions for $\lambda = 1.3$ mm show ~ 60 mJy for long East-West baselines and ~ 25 mJy for long North-South baselines [Johnson and Gwinn, 2015], assuming a Gaussian source of FWHM = 40 $\mu\text{-arcsec}$.

Distinguishing intrinsic source and ISM substructure and variability is an interesting challenge. Observations at mm-wavelengths have revealed deviations from the λ^2 scattering scaling law, see Fig. 2.3. This is interpreted as

due to the presence of intrinsic source structure and has been fitted with a power-law with an exponent of 1.34 ± 0.01 Lu et al. [2011]. This has enabled the constraint of various theoretical models Bower et al. [2006], excluding advection-dominated accretion flows (ADAF) ? and Bondi-Hoyle accretion ?. However observations extending over month timescales are required to properly sample the larger scale inhomogeneities and even with multiple epoch observations, it can be difficult to distinguish source and scattering characteristics [Macquart and Bower, 2006]. The developments in scattering theory presented above provide a robust mechanism for quantifying refractive effects. This could allow a decoupling without sampling a refractive ensemble but significant assumptions are always made on the source model.

2.2.3 Troposphere

The coherence and intensity of millimetre wavelength electromagnetic waves are most severely deteriorated in the lowest atmospheric layer, the troposphere which extends up to an altitude of $7 - 10$ km above sea level and down to a temperature $T \sim 218$ K [Thompson et al., 2001]. The troposphere is composed of a number of different components including primary gases N₂ and O₂, trace gases e.g. water vapour and CO₂, as well as particulates of water droplets and dust. The rest of this section will explore the tropospheric corruption for the mm-VLBI case beginning with insights from the fundamentals of electromagnetic propagation, followed by a review of atmospheric corruptions in the sub-mm regime. We then firm up our theory with a discussion on atmospheric radiative transfer and atmospheric turbulence.

Propagation fundamentals

Consider a quasi-monochromatic wave passing through a linear medium,

$$E_\nu(x, t) = E_0 \exp^{i(kn_\nu x - 2\pi\nu t)}, \quad (2.24)$$

where $k = 2\pi\nu/c$ is the propagation constant in free space and $n = n_R + jn_I$ is the complex index of refraction. Note that we will occasionally omit the frequency dependence of n and related quantities to simplify the notation. If n_I is nonzero, the electric flux I will decay exponentially

$$I = EE^* = E_0^2 \exp(-\tau), \quad (2.25)$$

where τ is called the opacity or optical depth and is related to the absorption coefficient, $d\tau = \kappa dx$ where $\kappa = 4\pi\nu n_I/c$. If $n_R > 1$ the phase velocity of light will decrease, $v_p = c/n_R$, which results in a time delay. The time delay due to the troposphere, \tilde{t} and opacity τ can be calculated simultaneously,

$$\tilde{t} + i\tau/4\pi\nu = 1/c \int_{path} d\mathbf{s} (n_\nu(\mathbf{s}) - 1). \quad (2.26)$$

In the interferometric context opacity and time delay are often viewed independently. However, the electric field is real and causal which imposes restrictions on the complex refractive index. Specifically n_R and n_I contain the same information and can be interchanged via the Kramers-Kronig relations.

Absorption is accompanied by emission and for a medium in local thermodynamic equilibrium, Kirchoff's law states that

$$\frac{\epsilon_\nu}{\kappa_\nu} = B_\nu(T), \quad (2.27)$$

where $\epsilon_\nu = dI_\nu/dx$ is the emission coefficient and $B_\nu(T)$ is the Planck function. Hence the absorbing molecules are also emitters, increasing system noise. Therefore opacity, time delay and atmospheric noise are interrelated and should be simulated consistently. On a side note these relations allow for phase calibration using measurements of sky emission via Water Vapour Radiometry (WVR) [e.g. Carilli and Holdaway, 1999].

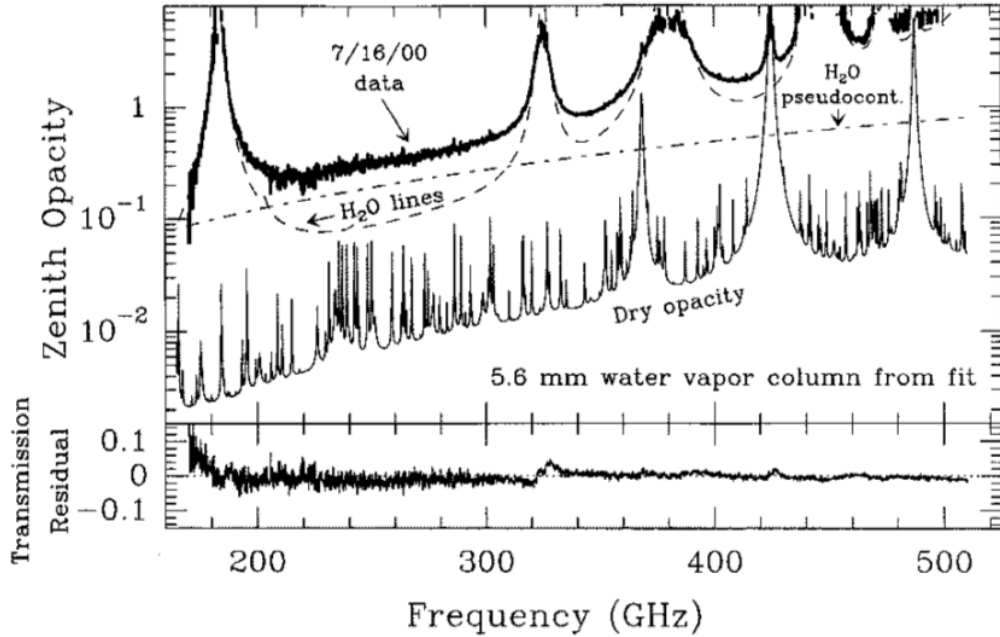


Figure 2.5: Recorded zenith absorption spectrum in the 160–520 GHz range, taken on Mauna Kea at an altitude of ≈ 4000 m. The data has been fit to a sum of H₂O lines, an H₂O pseudo-continuum and dry absorption lines. The model has been generated using the ATM code (see section 2.2.3), with the bottom panel showing the residuals. Here ‘dry’ refers to all atmospheric constituents except H₂O. Reproduced from Pardo et al. [2001]

Atmospheric corruptions in the (sub-)mm regime

An analysis of the absorption spectrum in the GHz range (Fig. 2.5), shows that it is dominated by transitions of H₂O and O₂ as well as a pseudo-continuum opacity which increases with frequency. The pseudo-continuum opacity is due to the cumulative effect of the far wings of a multitude of broadened water vapour lines above 1 THz [Carilli and Holdaway, 1999]. At 230 GHz the absorption is typically 5 – 10% at the best sites, during good weather.

In contrast to the dry atmospheric components, water vapour mixes

poorly and its time-variable spatial distribution induces rapid fluctuations in the time delays \tilde{t} above each station. The phase error for a baseline (1,2) where antenna 1 is the reference will be

$$\delta\phi(t, \nu) = 2\pi/\nu(\tilde{t}_2(t, \nu) - \tilde{t}_1(t, \nu)). \quad (2.28)$$

The water vapour column volume is measured as the depth of the column when converted to the liquid phase and is referred to as the precipitable water vapour (PWV). PWV is directly proportional to the time delay and hence the phase delay,

$$\delta\phi \approx \frac{12.6\pi}{\lambda} \times w, \quad (2.29)$$

where w is the depth of the PWV column [Carilli and Holdaway, 1999] and an atmospheric temperature $T = 270$ K has been assumed. This relationship between phase and water vapour content has been experimentally verified [Hogg et al., 1981]. At 230 GHz, the change in PWV needed to offset the phase by 1 rad is $\Delta w \approx 0.03$ mm.

This sensitive dependence of phase coherence on atmospheric stability is aggravated by three factors. First antenna elevation angles are typically fairly low for EHT observations which increases the atmospheric path length. Second as stations are far apart the atmospheric variations are uncorrelated between stations, this increases visibility decoherence as atmospheric variations appearing in both terms of equation 2.28 fall away. Third, observing with a sparse VLBI array means that there is less redundancy for calibration and so it is more difficult to separate source from atmospheric variations.

Radiative transfer

The problem of radiative transfer through a static atmosphere is well described and implemented by the Atmospheric Transmission at Microwaves (ATM) software [Pardo et al., 2001]. ATM has been incorporated into MEQSIL-

HOUETTE to provide a fast and sophisticated procedure to calculate average opacities, sky brightness temperatures and time delays. Here we provide a brief summary of the theory underpinning the package but refer the reader to Pardo et al. [2001] for more detail. ATM is commonly used in the Atacama Large Millimeter Array (ALMA) community [Curtis et al., 2009, Nikolic et al., 2013] and has been tested with atmospheric transmission spectra taken on Mauna Kea [Serabyn et al., 1998].

We start from the unpolarised radiative transfer equation, which is unidirectional in the absence of scattering,

$$\frac{dI_\nu(s)}{ds} = \epsilon_\nu(s) - \kappa_\nu(s)I_\nu(s), \quad (2.30)$$

where s is the coordinate along the signal path through the atmosphere. We assume local thermodynamic equilibrium (LTE) which should hold as the collisional timescale is much smaller than the time for spontaneous emission for all but the highest part of the atmosphere. Applying equation 2.27, multiplying by $\exp(-\tau_\nu)$ and integrating from the top of the atmosphere ($s = 0$) yields,

$$I_\nu(s) = I_\nu(0)e^{-\tau_\nu(0,s)} + \int_0^s B_\nu(s')e^{-\tau_\nu(s',s)}\kappa_\nu(s')ds', \quad (2.31)$$

where s' is a dummy variable in the same direction as s and $\tau_\nu(0,s) = \int_0^s k_\nu(s')ds'$. $I_\nu(0)$ is normally taken as the radiance from the cosmic background. To calculate the $I_\nu(s)$, $\tau(s)$ and complete the above integral, requires κ_ν as a function of altitude and frequency. The time delay \tilde{t} can be calculated from τ using the Kramers-Kronig relations.

A general equation to determine the absorption coefficient for a transition between a lower l and upper u states is given in the original paper. Here we merely point out that it should be proportional to the energy of the photon, $h\nu_{l \rightarrow u}$, the transition probability or Einstein coefficient, $B_{l \rightarrow u}$, the line-shape, $f(\nu, \nu_{l \rightarrow u})$ and the number densities N of electronic populations. Line profiles

which describe pressure broadening (perturbations to the Hamiltonian due to the presence of nearby molecules) and Doppler broadening are used. The condition of detailed balance further requires that decays from the upper state are included yielding, $g_u B_{u \rightarrow l} = g_l B_{l \rightarrow u}$, where g is the degeneracy of the electronic state. Putting this together we find,

$$\kappa(\nu)_{l \rightarrow u} \propto h\nu B_{l \rightarrow u} \left(\frac{N_l}{g_l} - \frac{N_u}{g_u} \right) f(\nu, \nu_{l \rightarrow u}), \quad (2.32)$$

where the Einstein coefficients are calculated from the inner product of the initial and final states with the dipole transition operator,

$$B_{l \rightarrow u} = \frac{2\pi}{3\hbar^2} | \langle u | \mu | l \rangle |^2, \quad (2.33)$$

where $|u\rangle$, $|l\rangle$, $|\mu\rangle$ are the wavefunctions of upper and lower states and the dipole transition operator respectively. The number densities of the two states, N_u and N_l in local thermodynamic equilibrium (LTE) are simply related to the local number density and temperature via Boltzmann statistics.

$$\frac{N_n}{N} = g_n \frac{\exp -\frac{E_n}{kT}}{Q} \quad (2.34)$$

where Q is the partition function. $Q = \sum_i g_i \exp -E_i/kT$. Transition lines at radio wavelengths result from rotational state transitions. To calculate the inner product given in equation 2.33, Operators which describe linearly symmetric rotors (e.g. O₂, CO) and asymmetric rotors are used. The asymmetric rotations are decomposed into three principal rotation axes with differing rotational constants governing each axis. Rotational constants were measured by the authors as well as drawn from a variety of literature. Partition functions and transition probability are calculated using approximations taken from the literature.

Far wing broadening of H₂O lines > 1.2 THz extends to lower frequencies and is not completely represented by the line-shape used. This is believed to

be due to self-self collisions of water molecules. Additionally there are terms from the dry atmosphere related to transient dipoles and Debye absorption which are not represented in the line-shape. To correct for these effects, two pseudocontinua are used. These are modelled as a power law dependence on frequency, temperature and the molecular densities.

Turbulent phase fluctuations

Visibility phase instability $\delta\phi(t)$ due to tropospheric turbulence is a fundamental limitation to producing high fidelity, science-quality maps with a mm-VLBI array [Thompson et al., 2001]. The coherence time-scale is typically too rapid ($\lesssim 10$ s) for fast switching calibration, so other calibration procedures (e.g. water vapour radiometry, paired antennas, and/or self-calibration) must be performed. Self-calibration is the most commonly used but is limited by the integration time needed to obtain adequate SNR to fringe fit. Phase decoherence often leads to the use of closure quantities to perform model fitting [Doeleman et al., 2001, Bower et al., 2004, Shen et al., 2005], and causes a decrease in measured flux due to incoherent complex averaging. In the section we will review and develop the weak scattering theory introduced earlier which will culminate in a formulation for the simulation of tropospheric phase turbulence seen by a mm-VLBI array. How this formulation is implemented and fits into the broader atmospheric simulation framework will be discussed in section 3.2.2.

Following from section 2.2.1, we model the statistics of $\delta\phi(t)$ with a thin, frozen, Kolmogorov-turbulent phase screen moving with a bulk velocity, v . However, the turbulent layer has a definite width Δh and both Kolmogorov theory and measurement [Fig. 2.6, Coulman, 1985, Treuhaft and Lanyi, 1987,

Carilli and Holdaway, 1997] show that this brings in a new regime

$$\beta = \begin{cases} 5/3 & \text{if } r < \Delta h, \\ 2/3 & \text{if } r > \Delta h, \\ 0 & \text{if } r > r_{\text{out}}. \end{cases} \quad (2.35)$$

In Fig. 2.6 we can see estimations of $\Delta h \approx 1$ km and $r_{\text{out}} \approx 6$ km. We will show later that even though we are working with a VLBI array, our implementation falls in into the $r \ll \Delta h$ regime.

We set the height h of the screen at the water vapour scale height of 2 km above ground. At 1.3 mm, the Fresnel scale is $r_F \approx 0.45$ m and experiments show annual variations of $r_0 \sim 50 - 500$ m above Mauna Kea [Masson, 1994] and $r_0 \sim 90 - 700$ m above Chajnantor [Radford and Holdaway, 1998], where both sites are considered to have excellent atmospheric conditions for millimetre astronomy. As $r_F < r_0$, this is an example of weak scattering.

The required field-of-view (FoV) of a global mm-VLBI array is typically $\text{FoV} < 1$ mas or $\sim 10 \mu\text{m}$ at a height of 2 km, which is roughly 7-8 orders of magnitude smaller than the tropospheric coherence length. The tropospheric corruption can therefore be considered constant across the FoV and, from the perspective of the Measurement Equation, modeled as a diagonal Jones matrix per time and frequency interval. As VLBI baselines are much longer than the coherence length, $|\mathbf{b}| \geq 1000$ km $\gg r_0$, the phase screen at each site must be simulated independently. This assumption only holds for VLBI baselines and the framework needs to be extended to simulate the effects of turbulence on individual phased arrays stations (e.g. SMA) and short (< 10 km) baselines (e.g. JCMT - SMA).

Our aim then is to produce a phase error time sequence $\{\delta\phi(t_i)\}$ for each station which is added to the visibility phase. We invoke the frozen screen assumption and write the structure function as a function of time, $D(t) = D(r)|_{r=vt}$. The temporal structure function $D(t)$ provides an efficient route to sample the variability of the troposphere at the typical integration

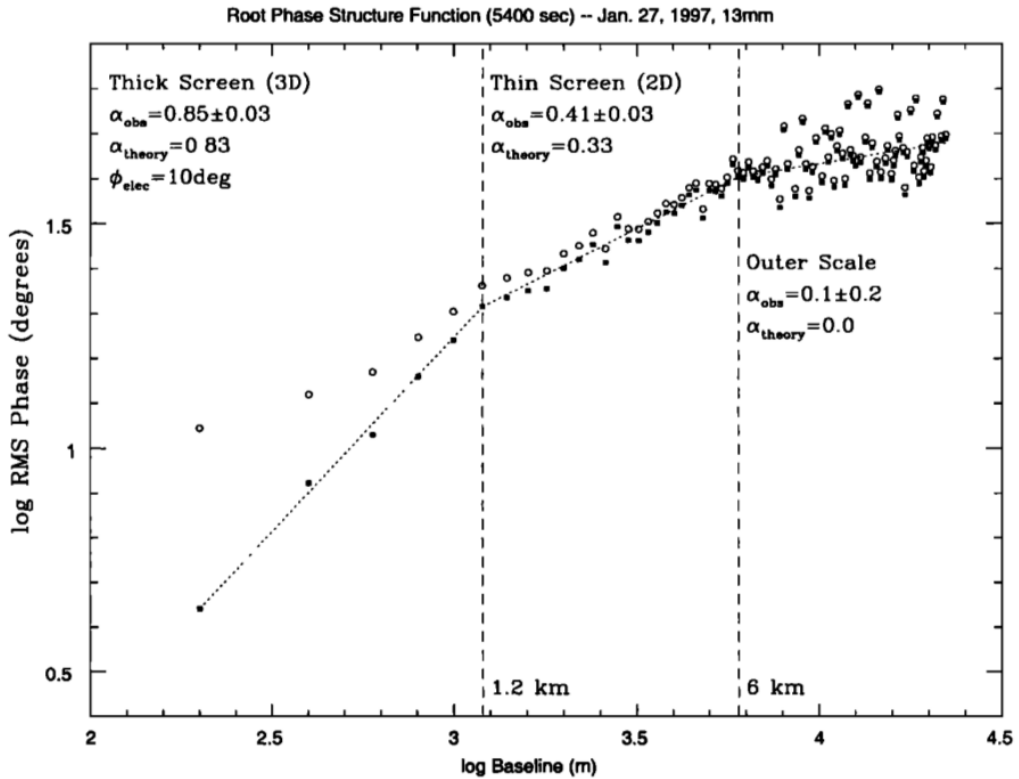


Figure 2.6: A log-log plot of RMS visibility phase versus baseline length for an observation of 1 Jy source 0748 + 240 with VLA at 22 GHz over a 90 min duration. The open circles show RMS phase as measured whereas the solid squares show the same values with a constant thermal noise contribution of 10° subtracted in quadrature. Note that the measured and theoretical Kolmogorov turbulent exponent β changes with distance on the phase screen as the viewing configuration transitions from a thick screen ($\beta_{\text{theory}} = 5/3$) to a thin screen ($\beta_{\text{theory}} = 2/3$) at $r \approx 1 \text{ km}$ and from a thin screen to completely uncorrelated regime ($\beta = 0$) beyond the outer scale at $r \approx 6 \text{ km}$. Although these regimes appear distinct, there is continuous variation between them. Reproduced from Carilli and Holdaway [1997]

time of the dataset, $t_{\text{int}} \sim 1$ sec.

The temporal variance of the phase is a function of the temporal structure function, and accounting for time integration yields [see Treuhhaft and Lanyi, 1987, B3]

$$\sigma_\phi^2(t_{\text{int}}) = (1/t_{\text{int}})^2 \int_0^{t_{\text{int}}} (t_{\text{int}} - t) D_\phi(t) dt. \quad (2.36)$$

Assuming power-law turbulence and integrating yields,

$$\sigma_\phi^2(t_{\text{int}}) = \left[\frac{1}{\sin \theta (\beta^2 + 3\beta + 2)} \right] \left(\frac{t_{\text{int}}}{t_0} \right)^\beta, \quad (2.37)$$

where $t_0 = r_0/v$ is the coherence time when observing at zenith and $1/\sin \theta$ is the approximate airmass which arises as $D_\phi \propto w$. As $r \ll \Delta h$, where Δh is the thickness of the turbulent layer, an thin screen exponent of $\beta = 5/3$ is justified [Treuhhaft and Lanyi, 1987]. The phase error time-series takes the form of a Gaussian random walk per antenna. At mm-wavelengths, the spectrum of water vapour is non-dispersive up to a few percent [Curtis et al., 2009] and so we can assume a simple linear scaling across the bandwidth.

Phase fluctuations $\delta\phi(t)$ can also be simulated by taking the inverse Fourier transform of the spatial phase power spectrum. However this approach is much more computationally expensive, e.g. for an observation length t_{obs} involving $N_{\text{ant}} = 8$ independent antennae with dish radii $r_{\text{dish}} = 15$ m, wind speed $v = 10$ m s⁻¹ and pixel size equal to r_F , the number of pixels $N_{\text{pix}} \approx N_{\text{ant}} t_{\text{obs}} r_{\text{dish}}^2 / (v r_F^3) \sim 10^8$. Additionally, due to fractal nature of ideal Kolmogorov turbulence, the power spectrum becomes unbounded as the wavenumber approaches zero which makes it difficult to determine the sampling interval of the spatial power spectrum [Lane et al., 1992].

2.2.4 Instrumental

All instruments suffer from both systematic and stochastic errors, the characterisation of which are essential to high precision measurement. In this

section we explore thermal noise (stochastic) and antenna pointing errors (systematic). While there are many additional potential sources of error (e.g. clock errors, bandpass, polarisation leakage, phasing errors, quantisation, correlator model, etc.). The point here is to demonstrate the mm-VLBI framework that enables more sophisticated interferometric simulations. The Measurement Equation formalism, enables any arbitrary linear error to be incorporated as a Jones Matrix e.g. a bandpass error would be a frequency-dependent diagonal Jones matrix.

Thermal Noise

The level of thermal noise of measurement defines the absolute limit on the sensitivity of the interferometer to detect a source and also to distinguish fine source characteristics. Closure quantities are especially prone to high levels of thermal as several visibilities are multiplied. A derivation of the thermal noise of an interferometer can be made through derivation of the thermal noise of an antenna and then correlating the result [Wrobel and Walker, 1999]. The RMS thermal noise of an interferometer $\{i, j\}$ over a bandwidth $\Delta\nu$ and an integration time is given by

$$\Delta S_{ij} = \frac{1}{\eta_s} \sqrt{\frac{SEFD_i SEFD_j}{2\Delta\nu t_{int}}}, \quad (2.38)$$

where η_s is the system efficiency and $2\Delta\nu t_{int}$ is the number of independent samples. The *SEFD* is a measure of the sensitivity of an antenna, accounting for the efficiency, collecting area and thermal noise and is defined as the flux density of a source with the same power,

$$SEFD = 2k_B T_{sys}/(\eta_a A), \quad (2.39)$$

where A is the antenna area, η_a is the antenna efficiency, T_{sys} is the system temperature and the factor $\frac{1}{2}$ accounts for only sampling 1 polarisation.

As the RIME was formulated for a thermal noise-free measurement, we

do not apply this corruption as a multiplicative matrix but rather an additive matrix,

$$\mathbf{V}_{pq} = \mathbf{G}_p \mathbf{X}_{pq} \mathbf{G}_q^H + \mathbf{N}_{pq}, \quad (2.40)$$

where each component of $N_{pq} \sim (0, \Delta S_{ij}^2)$.

Antenna Pointing

All antennas suffer pointing errors to some degree due to a variety of factors including dish flexure due to gravity, wind and thermal loading, as well as drive mechanics. This corresponds to an offset primary beam, which should only translate to minor amplitude errors if the pointing error θ_{PE} is significantly smaller than the primary beam (i.e. $\theta_{PE} \ll \theta_{PB}$). In the Measurement Equation formalism, this offset can be represented by a modified (shifted) primary beam pattern in the *E*-Jones term

$$\mathbf{E}_p(l, m) = \mathbf{E}(l_0 + \delta l_p, m_0 + \delta m_p), \quad (2.41)$$

where $\delta l_p, \delta m_p$ correspond to the directional cosine offsets. This could be a problem for millimetre observations as the primary beam is significant, e.g. for a 30 m dish at 1.3 mm, $\theta_{PB} \sim 10$ arcsec, compared to the $\theta_{PE} \sim 1$ arcsec.

We identify two main classes of pointing error. Firstly an antenna tracking a source will suffer a slow, continuous time-variable pointing error associated with the tracking error σ_{track} . Physically this could be attributed to changes in wind, thermal and gravitational loading which all change with telescope pointing direction and over the course of a typical few hour observation. Using the MeqTrees software package, such behaviour has been demonstrated to occur with the Westerbork Synthesis Radio Telescope (WSRT, Smirnov [2011c])¹.

Secondly, whilst a stationary phase centre is tracked, the pointing er-

¹See also <https://indico.skatelescope.org/event/171/session/9/contribution/20>

rror should evolve slowly and smoothly, however, in mm-VLBI observations the phase centre is often shifted to another source/calibrator. This would cause the pointing error to change abruptly, with an absolute pointing error $\sim \sigma_{\text{abs}}$. Source/calibrator change is scheduled every 5-10 minutes in a typical millimetre observation. The point is that even though EHT will be able to determine the pointing offset when observing a calibrator with well known structure, when the antennas slew back to a source (e.g. Sgr A*) with less certain or variable source structure, the pointing error could change significantly. This is exacerbated by the scarcity of mm-wavelength calibrators, which are often widely separated from the source.

Chapter 3

Software implementation

3.1 Design objectives

Our primary aim is to test and research mm-VLBI calibration, imaging and parameter estimation algorithms/strategies through the construction of a synthetic data simulation framework. To address the many questions within the wide scope of this objective, one must be able to setup and run a diversity of experiments within the simulation framework. This places definite constraints on the software architecture. In particular, the framework should

- enable the implementation of all relevant classes of signal corruption within a formalism which ensures consistency with the causal signal transmission chain,
- be compatible with time-variable GRMHD source models which are to be used as inputs,
- be organised in modularised structure so that it is flexible, extendable and could be incorporated by other interferometric algorithms e.g. a calibration or a parameter estimation algorithm,
- The modular structure should also enable the construction and execution of arbitrary observations.

3.2 Architechture and Workflow

In this section, we will review how the architechural design and workflow of the simulator architechture has been designed to meet the above objectives. To fulfill the first objective, we try to cast signal corruptions in the RIME formalism (see section 2.1.1). Where this is not possible, i.e. for processes which can not be described with Jones matrix, to fit those signal corruptions into the casually correct position in the signal transmission chain, with proper consider given to non-communitivity of elements in the signal transmission path. The implementation of each signal corruption is described in the following subsections. The remaining objectives fall into the realm of software design and will be discussed in this subsection.

We have chosen to write the high level simulation code using the **PYTHON** language. **PYTHON** is a general purpose language, is geared towards readability, and is well supported by a comprehensive library and wide user base (including astronomers). Specifically **PYTHON** interfaces well with a modern interferometric toolbox, **MEQTREES**, as well as our data formats of choice: **FITS** for image cubes and the **MEASUREMENT SET**¹ **MS** for visibilities. Although the higher level functionality is written in **PYTHON**, the bulk of the computational load (**MS** and visibility generation) is called through subroutines which are written in the faster **C++** language. We use **MS** as our data format as it is directly accessible via the **PYRAP** library and is the data format used by **MEQTREES** which performs the visibility generation and pointing error simulation. Although in the mm-VLBI subfield other data formats are currently still more popular than the **MS**, i.e. **UVFITS** or **IOFITS**, but with the completion of ALMA, the **MS** format should become the next modern data format and is already in use at the Joint Institute for VLBI in Europe (JIVE).

To create a flexible and modular structure necessary to be able to run

¹<https://casa.nrao.edu/Memos/229.html>

a diversity of experiments, the software implementation is divided into 2 components:

- an object-oriented framework into which is programmed the logic of each individual step in the signal propagation chain,
- a driver script which initialises the most abstract class in the framework with the required inputs and determines the signal propagation chain relevant to that particular pipeline.

The conceptual flow diagram of one realisation of a MEQSILHOUETTE simulation pipeline is shown in Fig. 3.1. To emphasise, the framework is not restricted to this sequence of operations, allowing the exact pipeline to be quite general. This flexibility is made possible through extensive Object-Orientation.

All inputs to the simulator are specified by a configuration file, containing a dictionary, which is the sole input to the driver script. This dictionary contains everything needed by the pipeline to determine the particular observation configuration (frequency, bandwidth, start time, etc), which signal corruption implementation should be employed and where the sky model and antenna table are located in the filesystem. The antenna table is in the CASA format, and can readily be created or altered using the PYRAP library using the station coordinates. The primary sky model used is a time-ordered list of FITS images, where each image represents the source total intensity over a time interval $\Delta t_{\text{src}} = t_{\text{obs}}/N_{\text{src}}$, where t_{obs} is the observation length and N_{src} is the number of source images. Currently the pipeline only supports total intensity and the conversion of the pipeline to support full stokes is discussed in section ???. A variation of the pipeline has also been written which uses a parametric source model consisting of Gaussians or point sources as the sky model. This functionality was needed for the simulation of pointing errors as the MEQTREES beams model does not support the FITS sky model.

The primary outputs of the pipeline are an interferometric dataset in MS format along with the closure phases (including uncertainties) and a dirty

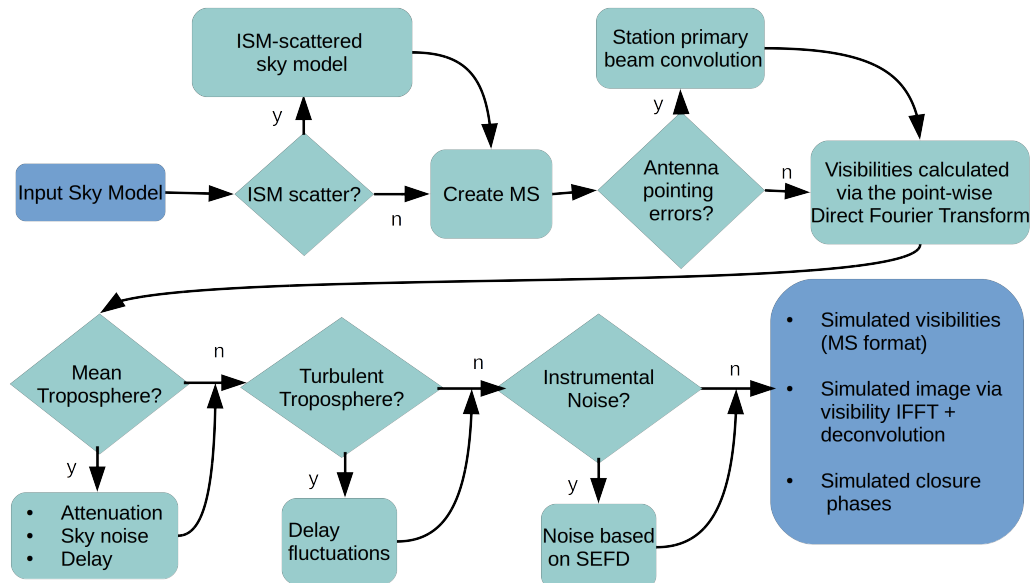


Figure 3.1: Flow diagram showing basic sequence of a MEQSILHOUETTE simulation pipeline. The specific sequence is determined by the driver script whereas the logic of each step is contained in an object-oriented framework. The details of the station information, observation strategy, tropospheric and ISM conditions are specified in a user-defined input configuration file. The pipeline is extendable, allowing any additional, arbitrary Jones matrices to be incorporated.

and/or deconvolved image. The modular structure of the pipeline allows for additional imaging and deconvolution algorithms to be easily appended to the final data processing steps. Noting that there are other data formats widely used in mm-VLBI, we make use of the CASA task for conversion to UVFITS. Similarly other data products can be easily produced as needed e.g. polarisation ratios.

An important step to reproduce realistic observations is to be able to create a comprehensive MS with arbitrary scan lengths, start times, channel and bandwidth structure. This is performed using the SIMMS² tool. SIMMS pro-

²<https://github.com/radio-astro/simms>

vides an easy to use command line interface to construct a general MS, given the appropriate antenna table. The call to SIMMS is located within the driver script.

In order to make the framework as clean and modular as possible we have made extensive use of object orientation. The first major class, *SimpleMS*, was intended to abstract and modularise the MS and MS-only derived attributes (e.g. visibility data and station positions) and methods (e.g. functions to calculate station elevations and closure phases) as well as expose these attributes and methods more efficiently than following PYRAP procedures which become verbose when used frequently. This is especially useful when accessing baseline-indexed quantities.

The second MS-related class, *TropMS*, handles the calculations relevant to tropospheric and thermal noise corruptions. This class is a child of *SimpleMS* and is initialised with weather and station information. Note that a child contains all the methods and attributes of its parent. This allows the tropospheric corruption implementation to use, whilst being separated from, the core MS functionality. The details of the tropospheric corruption is provided in section 3.2.2.

The third MS-related class, *SimCoordinator*, is a child of the *TropMS* class. *SimCoordinator* is designed to make arbitrary simulations easy and efficient to construct and execute on a high level. It is the only MS class directly initialised in the driver script and hence the low level functionality and attributes of its parents are abstracted from the user. In addition to inherited functionality, *SimCoordinator* can call the ISM-scattering task (see subsection 3.2.1), and MEQTREES simulation functionality. Specifically within MEQTREES we make use of the *turbo-sim* script which evaluates the RIME to generate visibilities and to simulate antenna pointing errors(see section 3.2.3), where the visibilities are calculated through direct evaluation of the Fourier Transform at each UVW coordinate in the dataset. MEQTREES allows its tasks to be called by a PYTHON function and so is naturally included in the pipeline.

Table 3.1: The list of the parameters, aside from the source model, needed to initialise and run SCATTERBRANE. Time variability is made possible as N_{pix} can be a 2-tuple (i.e. a rectangular screen can be created).

r_0	N_{pix}
r_{in}	principal angle
r_{out}	anisotropy of scattering kernel
D_{os}	λ
R	β
	screen resolution

3.2.1 ISM scattering

As described in section ?? observations of Sgr A* at sub(mm) is subject to ISM scattering in the strong scattering regime. Due to the size of Sgr A* at mm-wavelengths, a single epoch observation of the scattering screen is further defined as falling into the *average regime*, wherein diffractive scintillation is averaged out but refractive scintillation is still present. As mm-VLBI observations can resolve the scatter-broadened image of Sgr A*, an implementation of scattering is needed which approximates the subtle changes in its extended source structure. Such an approximation has been implemented in the PYTHON-based SCATTERBRANE³ package, and is based on Johnson and Gwinn [2015]. In this algorithm a phase screen is created based on the two dimensional spatial power spectrum [see Johnson and Gwinn, 2015, Appendix C] which incorporates inner and outer turbulent lengths scales. With the screen generated, the original image is scattered according to equation 2.21. In practice equation 2.21 is implemented using an interpolation function which is modified by the values on the phase screen. SCATTERBRANE allows variation in all parameters (see table 3.2.1) associated with the scattering screen which is essential as aspects of the scattering towards the galactic centre are still unconstrained.

We include the SCATTERBRANE software, which has already yielded im-

³<http://krosenfeld.github.io/scatterbrane>

portant context for mm-VLBI observations towards Sgr A^{*} [e.g. Ortiz-León et al., 2016], within the MEQSILHOUETTE framework. Our ISM module interfaces the SCATTERBRANE code within an interferometric simulation pipeline. This module enables simultaneous use of time-variable ISM scattering and time-variable intrinsic source structure within a single framework. The user is able to select a range of options relating to the time-resolution and epoch interpolation/averaging of both. By default, if the time resolution chosen to sample the source variability Δt_{src} and screen variability Δt_{ism} are unequal, we set

- $\Delta t_{\text{ism}} = \Delta t_{\text{src}}$ if $\Delta t_{\text{src}} < \Delta t_{\text{ism}}$
- $\Delta t_{\text{ism}} = R(\frac{\Delta t_{\text{src}}}{\Delta t_{\text{ism}}})\Delta t_{\text{src}}$ if $\Delta t_{\text{src}} > \Delta t_{\text{ism}},$

where R rounds the fraction to the nearest integer. This modification to the ISM sampling resolution avoids interpolation between different snapshots of the intrinsic source structure.

3.2.2 Atmospheric corruption simulator

Our focus in this module is to model the three primary, interrelated (see section 2.2.3) observables which are the most relevant to mm-VLBI: turbulence-driven fluctuations in the visibility phase $\delta\phi$; signal attenuation due to the atmospheric opacity τ ; and the increase in system temperature due to atmospheric emission at a brightness temperature T_{atm} . Our approach is to model these observables as being separable into mean and turbulent components which are simulated independently. The mean tropospheric simulation module performs radiative transfer with a detailed model of the electromagnetic spectrum of each atmospheric constituent. The turbulent simulation module takes a scattering approach to account for the decoherence that results from power-law turbulence.

As described in section 2.2.3, we use the ATM package to perform radiative transfer through the realisation of the mean atmosphere. In order to calculate atmospheric temperature and pressure profiles, ATM is input several station dependent parameters, namely, ground temperature and pressure, PWV depth, water vapour scale height, tropospheric lapse rate and altitude. The lapse rate refers to the linear relation at which temperature decreases with height. Through experimentation, we have found that the first 3 variables most significantly effect the results of the simulation and opt to keep the latter variables at their default values which were set for application to ALMA. The outputs of this procedure are mean values for opacity, time delay and atmospheric brightness temperature at each station. Both opacity and time delay are separated into wet (water) and dry components. These outputs are calculated for a list of frequencies. We perform this calculation using representative climate conditions taken from the literature. This final step is to account for elevation effects by multiplying by the airmass $1 / \sin \theta$.

Following from section 2.2.3, we derive a weak scattering formalism to calculate station dependent visibilities phase variations which result from observing through a turbulent troposphere. Specifically we simulate random walks in visibility phase with variance given by equation 2.37 for each antenna. These phase-time series are combined to form a multiplicative complex gain corruption, with amplitude of unity i.e. a diagonal Jones matrix. In section 4.1 we explore the effect of the mean and turbulent atmosphere on observables.

3.2.3 Pointing error simulator

To simulate pointing errors, we use the implementation built into the MEQTREES turbo-sim task. This functionality includes the capability to convolve station primary beams with the sky model. The beam models available through this function are sinc, Gaussian and the analytic WSRT beam model, however there is not much difference between the different beam models up until the

first null. The standard beam model which we will make use is the analytic WSRT beam model [Popping and Braun, 2008]

$$E(l, m) = \cos^3(C\nu\rho), \quad \rho = \sqrt{\delta l_p^2 + \delta m_p^2} \quad (3.1)$$

where C is a constant, with value $C \approx 130 \text{ GHz}^{-1}$. Note that the power beam EE^H becomes \cos^6 , resulting in a FWHM = 6.5 arcsec at 230 GHz. One drawback of the MEQTREES implementation is that it is incompatible with the FITS format and so we are limited to point and Gaussian parameteric sources for the pointing error simulations. However this is not a significant issue as the pointing error should be constant across the FOV and hence source structure observable with mm-VLBI is unimportant to any pointing error analysis.

Furthermore turbo-sim allows constant offset or time variable primary beam, where the time variability can be either an up-to-third order polynomial or a sinusoidal function. We have opted to incorporate only the sinusoidal variability for simplicity. To simulate stochastic variability i.e. pointing error due to slew between calibrator and source, we use a constant offset which is resampled per user-specified time interval. In section 4.1 we demonstrate the effect of constant, sinusoidally variable and stochastically variable pointing errors on the LMT which is the EHT station with the most narrow beam, and could be used as a referenced station due to its centrality the array.

3.3 RODRIGUES interface

For community use, we host the online, RODRIGUES, interface, found at <http://rodrigues.meqtrees.net/>. Each of the components of the simulator run in Docker containers. **Looks like the infrastructure is going to change, re: discussions with Gijs and Sphe, so going to wait before writing this.

Chapter 4

Results and analysis

We begin this section with canonical results from the simulator, exploring the crux of all signal corruptions implemented. Following this, we contrast these results to real VLBA 87GHz observations of Sgr A* and calibrators. In this analysis, we focus identifying ISM and tropospheric contributions to the data. We end with more sophisticated results of calibrator and imaging tests of a variable source within the context of a variable troposphere, with possibly some ISM thrown in.

4.1 Canonical simulations

4.1.1 ISM

To demonstrate the implementation and provide an example of intraday ISM variability, we present the results of a simulated observation of 10 minutes duration at 14:00 UTC on four consecutive days in Fig. 4.1. To compare to published observations, we use the three-station EHT array consisting of the Submillimeter Telescope (SMT) in Arizona, the Combined Array for Research in Millimeter-wave Astronomy (CARMA) in California and the James Clerk Maxwell Telescope (JCMT) on Mauna Kea, Hawaii. The distance to the screen is taken as $D_{\text{os}} = 5.8 \pm 0.3$ kpc [Bower et al., 2013]. The rela-

tive transverse velocity between the observer and scattering screen is set to 50 km s^{-1} to be consistent with Ortiz-León et al. [2016]. The source is a circular Gaussian with a $\text{FWHM} = 40 \mu\text{-arcsec}$, approximately the angular distance that a scattering screen would travel over ~ 4 days. The source size has been chosen such that it is consistent with the latest estimate of the size of Sgr A* at 230 GHz [Fish et al., 2011]. Closure quantities are model dependent and calculated as specified in Rogers et al. [1995], where the thermal noise was added based on the system equivalent flux density (SEFD) table in [Lu et al., 2014]. The ISM scattering implementation `SCATTERBRANE`, based on Johnson and Gwinn [2015], has been incorporated into the pipeline. Fig. 4.1 provides an example of closure phase and flux variability over a 4 day period using a static source. Accurate simulation of the ISM-induced closure phase variation is essential in order to make any inference on asymmetric, event-horizon scale structure [e.g. Fish et al., 2016, Ortiz-León et al., 2016]. This will become even more important as the EHT sensitivity increases by an order of magnitude in the near future. Note that if the source has intrinsic spatial variability as in the case of a hotspot model Doeleman et al. [2009], this will increase ISM variability as the relative motion between source, screen and observer is increased.

4.1.2 Atmospheric

Typical opacities and sky brightness temperatures for ALMA, the Submillimeter Array (SMA) and the South Pole Telescope (SPT) are shown in Fig. 4.2. Note that both the opacity and brightness temperature are inversely proportional to the ground temperature and proportional to ground pressure.

In section ?? we explore the observational consequences of observing through a turbulent troposphere. In this simulation, we assume a simple point source model and apply increasing levels of turbulence-induced phase fluctuations before imaging using the two dimensional inverse fast Fourier

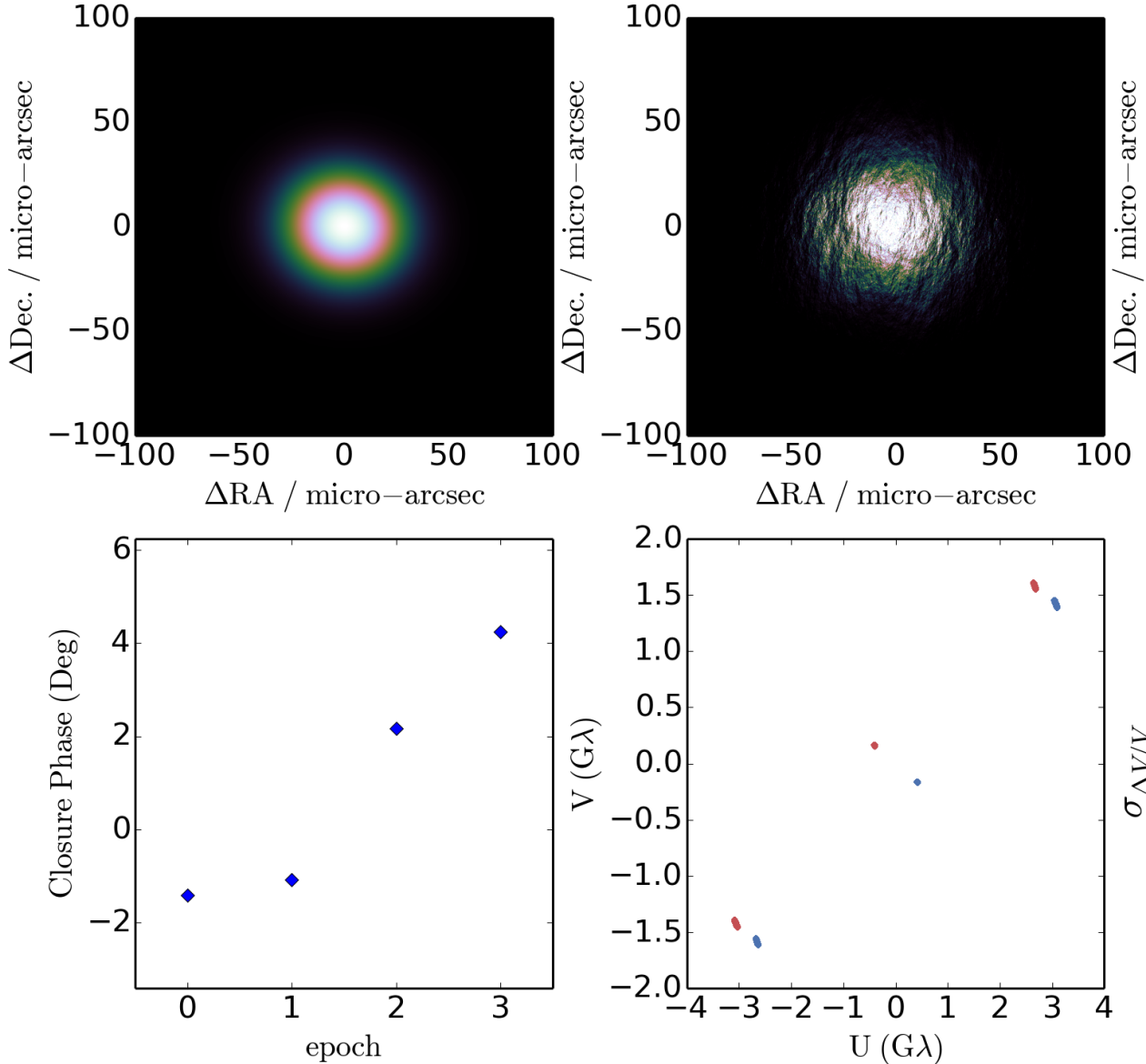


Figure 4.1: An example simulation of ISM scattering towards Sgr A*, observed with SMT-JCMT-CARMA. The top panel, left to right, shows the original $\text{FWHM} = 40 \mu\text{-arcsec}$ Gaussian (**top left**), the simulated ISM scattered image on the first night (**top middle**) and last night (**top right**) of the observation, respectively. The bottom panel, left to right, shows the evolution of the 10 minute-averaged closure phase with epoch (**bottom left**), uv-tracks for each night (**bottom middle**) and the RMS fractional visibility amplitude differences $\sigma_{\Delta V}/V_{\text{ea}}$ as a function of uv -distance (**bottom right**). $\Delta V = (|V_a| - |V_{\text{ea}}|)$, where $|V_a|$ and $-|V_{\text{ea}}|$ are the simulated average and ensemble average visibility amplitudes respectively. Variations from the ensemble-average flux on the shortest baselines reveal total flux modulation while flux variations on longer baselines and non-zero closure phases track the fluctuations in substructure. Furthermore, ISM scattering simulations can constrain the variability fraction associated with the screen, enabling a characterization of the variability as demonstrated in Optic Lá.

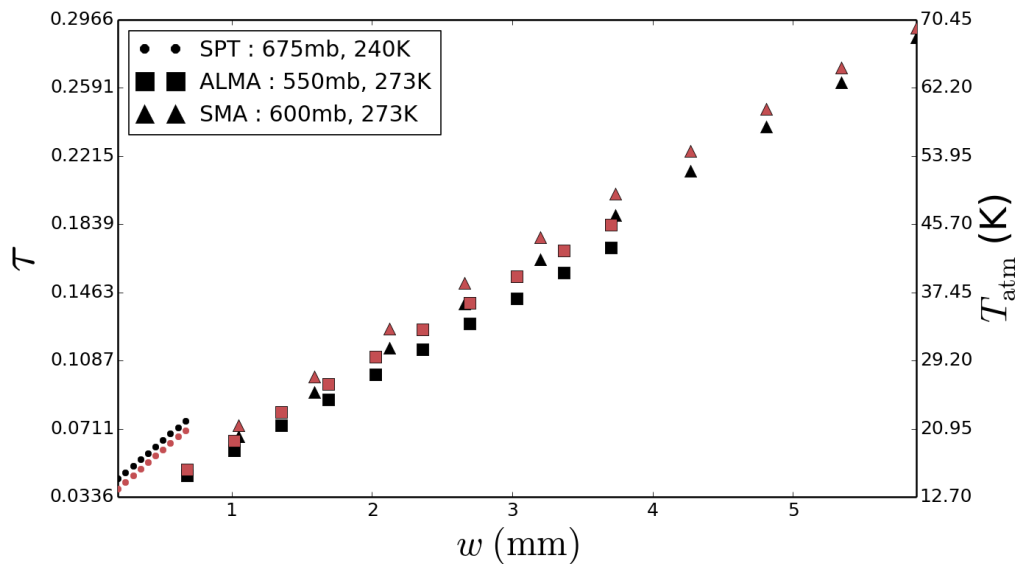


Figure 4.2: Simulated mean opacity (black) and sky brightness temperature (red) at $\nu = 230$ GHz for three typical ground pressures and temperatures over a typical PWV range [Lane, 1998] which approximately represent the sites of SPT (dots), ALMA (squares) and SMA (triangles). The legend shows the estimated input ground (pressure, temperature) parameters for each site.

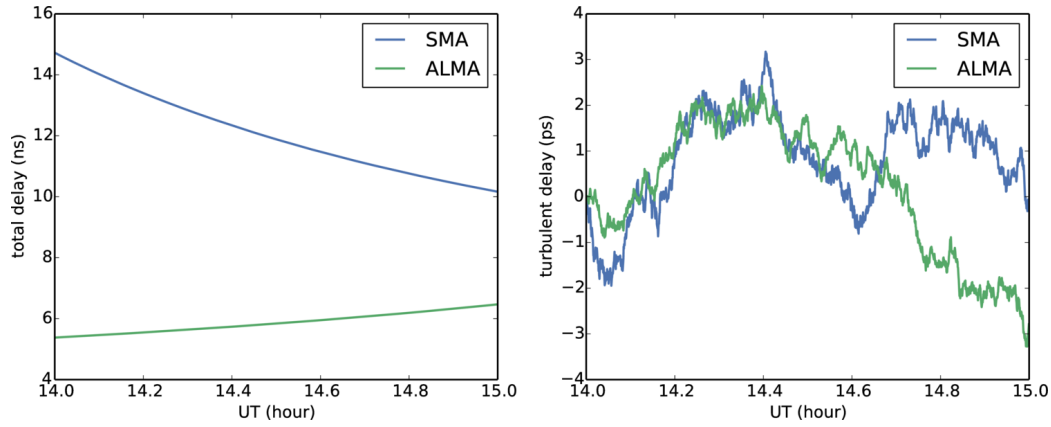


Figure 4.3: Simulation of the total delay (left) and the turbulent atmospheric delay (right) for SMA (blue) and ALMA (green) sites towards Sgr A*. Ground pressures and temperatures are the same as Fig. 4.2, precipitable water vapour above each station is set to $w = 2$ mm, and the instantaneous zenith coherence time is set $T_0 = 10$ s for both stations. Note that all tropospheric parameters are, however, independently set. The conversion from time delay to phase at 230 GHz is 1 rad = 0.7 ps.

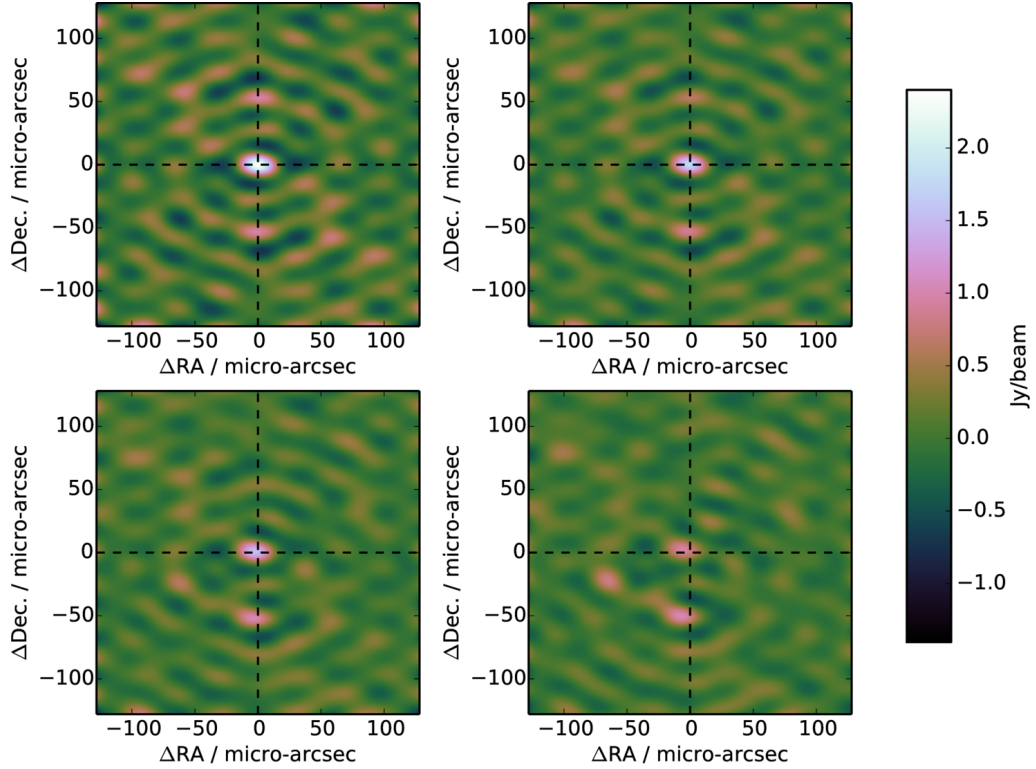


Figure 4.4: The effect of residual troposphere phase noise on interferometric images of a point source observed for 12 hours at 230 GHz with 4 GHz bandwidth with the following array : SPT, ALMA, SMA, SMT, LMT and JCMT, assuming the same SEFDs as Lu et al. [2014] and an elevation limit of 15° . For simplicity the weather parameters at each station were set to: coherence time $t_0 = 10$ sec; PWV depth $w = 1$ mm; ground pressure $P = 600$ mb; ground temperature $T = 273$ K. **Top left:** interferometric map with thermal noise only. **Top right:** atmospheric attenuation and sky noise (due to non-zero opacity) with 1% of the turbulent phase noise added. **Bottom left:** as previous but with 3% of turbulent phase contribution. **Bottom right:** as previous but with 6% turbulent phase contribution. The fractional turbulent phase contributions are illustrative of the effect of fringe-fitting errors. Note the decrease in the source peak flux with increasing turbulent tropospheric phase noise. Note further that the peak source centroid is offset from its true position (black crosshairs).

transforms. We note a rapid attenuation in peak flux due to incoherent averaging, slight offsets in the source centroid and the presence of spurious imaging artefacts. Surprisingly, in this configuration, there was no evidence of blurring or a loss of resolution with the uncertainties. In an upcoming paper, we perform a systematic exploration of the turbulent tropospheric effects on the accuracy of fringe-fitting algorithms/strategies, through use of an automated calibration procedure and including the added complexity of a time-variable source.

4.1.3 Pointing

In section ??, we show how antenna pointing errors of the LMT could introduce fractional RMS amplitude variations $\sigma_{\Delta V/V_0} \leq 0.4$ on the timescale of phase centre switching. This would occur if the calibrator is widely separated from the source, as is often the case in mm-VLBI. In contrast tracking errors are less problematic with $\sigma_{\Delta V/V_0} \leq 0.05$. If the gain error is non-separable from the calibration model used, it could be interpreted as intrinsic variability, substructure and/or increased noise. If unaccounted for, this effect has the potential to limit the dynamic range of mm-VLBI images. Further tests to constrain the pointing uncertainties of EHT stations will lead to more accurate interferometric simulations and hence the overall impact on black hole shadow parameter estimation. Here we demonstrate the capability to incorporate a range of plausible pointing error effects into a full simulation pipeline.

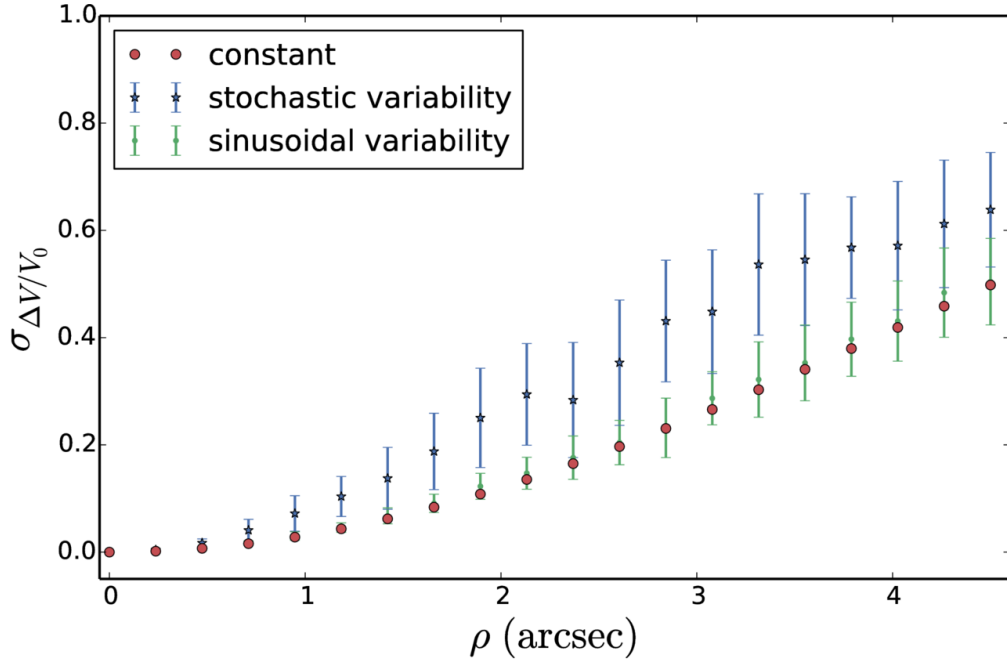


Figure 4.5: RMS relative amplitude error induced by pointing error with the 50 m (i.e. fully illuminated) LMT antenna as a function of pointing error offset ρ at 230 GHz. We assume that these errors are degenerate or non-separable from the self-calibration/fringe-fitting model used. See text for the description of the three models used. This simulation capability enables constraints on the magnitude of pointing-induced errors given a particular pointing calibration strategy.

4.2 Calibration and imaging of a time variable source in the presence of the troposphere

First we fringe fit and image a stationary point source and compare to the result in Fig. 4.4.

Chapter 5

Conclusion and future work

In light of the science objectives of mm-VLBI observations and software advances in the broader radio interferometry community, a mm-VLBI data simulator has been developed. An important feature is that this simulation pipeline is performed using the MEASUREMENT SET format, in line with ALMA and future VLBI data formats. The focus has been placed on simulating realistic data given an arbitrary theoretical sky model. To this end, the simulator includes signal corruptions in the interstellar medium (ISM), troposphere and instrumentation. Examples of typical corruptions have been demonstrated, which show that each corruption can significantly affect the inferred scientific parameters. Particular focus has been placed on EHT observations, however, the pipeline is completely general with respect to observation configuration and source structure. Time variability in all domains (source, array, ISM, troposphere) is implemented. Future releases of MEQSILHOUETTE will include polarisation dependent corruptions. The creation of a close interface between sophisticated theoretical and interferometric mm-VLBI simulations will enhance the scientific opportunities possible with the EHT.

Significant progress has been made in the theoretical and numerical modeling of the inner accretion flow and jet launch regions near a supermassive black hole event horizon. With MEQSILHOUETTE, we now have the ability to

couple these with sophisticated interferometric and signal propagation simulations. This offers a tool to enable a more closely-knit and effective interplay between theoretical predictions and observational capabilities. Moreover, detailed interferometric simulations will enable us to quantify systematic effects on the black hole and/or accretion flow parameter estimation.

Bibliography

- J. W. Armstrong, B. J. Rickett, and S. R. Spangler. Electron density power spectrum in the local interstellar medium. *ApJ*, 443:209, apr 1995. doi: 10.1086/175515. URL <http://dx.doi.org/10.1086/175515>.
- F. K. Baganoff, M. W. Bautz, W. N. Brandt, G. Chartas, E. D. Feigelson, G. P. Garmire, Y. Maeda, M. Morris, G. R. Ricker, L. K. Townsley, and F. Walter. Rapid X-ray flaring from the direction of the supermassive black hole at the Galactic Centre. *Nature*, 413:45–48, September 2001. doi: 10.1038/35092510.
- G. Bélanger, R. Terrier, O. C. de Jager, A. Goldwurm, and F. Melia. Periodic Modulations in an X-ray Flare from Sagittarius A*. *Journal of Physics Conference Series*, 54:420–426, December 2006. doi: 10.1088/1742-6596/54/1/066.
- T. Blecher, R. Deane, G. Bernardi, and O. Smirnov. MeqSilhouette : A mm-VLBI observation and signal corruption simulator. *ArXiv e-prints*, August 2016.
- Max Born and Emil Wolf. Principles of optics. *Pergamon, New York*, 1980.
- K. L. Bouman, M. D. Johnson, D. Zoran, V. L. Fish, S. S. Doeleman, and W. T. Freeman. Computational Imaging for VLBI Image Reconstruction. *ArXiv e-prints*, dec 2015.

- G. C. Bower, H. Falcke, R. M. Herrnstein, J.-H. Zhao, W. M. Goss, and D. C. Backer. Detection of the Intrinsic Size of Sagittarius A* Through Closure Amplitude Imaging. *Science*, 304:704–708, April 2004. doi: 10.1126/science.1094023.
- Geoffrey C. Bower, W. M. Goss, Heino Falcke, Donald C. Backer, and Yoram Lithwick. The Intrinsic Size of Sagittarius A* from 0.35 to 6 cm. *ApJ*, 648(2):L127–L130, aug 2006. doi: 10.1086/508019. URL <http://dx.doi.org/10.1086/508019>.
- Geoffrey C Bower, Adam Deller, Paul Demorest, Andreas Brunthaler, Ralph Eatough, Heino Falcke, Michael Kramer, KJ Lee, and Laura Spitler. The angular broadening of the galactic center pulsar sgr j1745-29: A new constraint on the scattering medium. *ApJ*, 780(1):L2, 2013.
- C. D. Brinkerink, C. Müller, H. Falcke, G. C. Bower, T. P. Krichbaum, E. Castillo, A. T. Deller, S. S. Doeleman, R. Fraga-Encinas, C. Goddi, A. Hernández-Gómez, D. H. Hughes, M. Kramer, J. Léon-Tavares, L. Loinard, A. Montaña, M. Mościbrodzka, G. N. Ortiz-León, D. Sanchez-Arguelles, R. P. J. Tilanus, G. W. Wilson, and J. A. Zensus. Asymmetric structure in Sgr A* at 3 mm from closure phase measurements with VLBA, GBT and LMT. *MNRAS*, 462:1382–1392, October 2016. doi: 10.1093/mnras/stw1743.
- A. E. Broderick, V. L. Fish, S. S. Doeleman, and A. Loeb. Constraining the Structure of Sagittarius A*'s Accretion Flow with Millimeter Very Long Baseline Interferometry Closure Phases. *ApJ*, 738:38, September 2011. doi: 10.1088/0004-637X/738/1/38.
- Avery E. Broderick and Abraham Loeb. IMAGING THE BLACK HOLE SILHOUETTE OF M87: IMPLICATIONS FOR JET FORMATION AND BLACK HOLE SPIN. *ApJ*, 697(2):1164–1179, may 2009. doi: 10.1088/

- 0004-637x/697/2/1164. URL <http://dx.doi.org/10.1088/0004-637x/697/2/1164>.
- Avery E. Broderick, Tim Johannsen, Abraham Loeb, and Dimitrios Psaltis. TESTING THE NO-HAIR THEOREM WITH EVENT HORIZON TELESCOPE OBSERVATIONS OF SAGITTARIUS A*. *ApJ*, 784(1):7, feb 2014. doi: 10.1088/0004-637x/784/1/7. URL <http://dx.doi.org/10.1088/0004-637x/784/1/7>.
- Avery E. Broderick, Vincent L. Fish, Michael D. Johnson, Katherine Rosenfeld, Carlos Wang, Sheperd S. Doeelman, Kazunori Akiyama, Tim Johannsen, and Alan L. Roy. MODELING SEVEN YEARS OF EVENT HORIZON TELESCOPE OBSERVATIONS WITH RADIATIVELY INEFFICIENT ACCRETION FLOW MODELS. *ApJ*, 820(2):137, mar 2016. doi: 10.3847/0004-637x/820/2/137. URL <http://dx.doi.org/10.3847/0004-637x/820/2/137>.
- C. L. Carilli and M. A. Holdaway. Tropospheric phase calibration in millimeter interferometry. *Radio Science*, 34(4):817–840, jul 1999. doi: 10.1029/1999rs900048. URL <http://dx.doi.org/10.1029/1999rs900048>.
- CL Carilli and MA Holdaway. Application of Fast Switching Phase Calibration at mm Wavelengths on 33 km Baselines. *MMA/ALMA Memorandum Series No 173, NRAO*, 1997.
- A. A. Chael, M. D. Johnson, R. Narayan, S. S. Doeelman, J. F. C. Wardle, and K. L. Bouman. High Resolution Linear Polarimetric Imaging for the Event Horizon Telescope. *ArXiv e-prints*, May 2016.
- C. E. Coulman. Fundamental and Applied Aspects of Astronomical “Seeing”. *Annual Review of Astronomy and Astrophysics*, 23(1):19–57, sep 1985. doi: 10.1146/annurev.aa.23.090185.000315. URL <http://dx.doi.org/10.1146/annurev.aa.23.090185.000315>.

- Emily I Curtis, Bojan Nikolic, John S Richer, and Juan R Pardo. Atmospheric dispersion and the implications for phase calibration. *arXiv preprint arXiv:0912.2852*, 2009.
- S. Doeleman, E. Agol, D. Backer, F. Baganoff, G. C. Bower, A. Broderick, A. Fabian, V. Fish, C. Gammie, P. Ho, M. Honman, T. Krichbaum, A. Loeb, D. Marrone, M. Reid, A. Rogers, I. Shapiro, P. Strittmatter, R. Tilanus, J. Weintroub, A. Whitney, M. Wright, and L. Ziurys. Imaging an Event Horizon: submm-VLBI of a Super Massive Black Hole. In *astro2010: The Astronomy and Astrophysics Decadal Survey*, volume 2010 of *Astronomy*, 2010.
- S. S. Doeleman, Z.-Q. Shen, A. E. E. Rogers, G. C. Bower, M. C. H. Wright, J. H. Zhao, D. C. Backer, J. W. Crowley, R. W. Freund, P. T. P. Ho, K. Y. Lo, and D. P. Woody. Structure of Sagittarius A* at 86 GH[CLC]z[/CLC] using VLBI Closure Quantities. *AJ*, 121(5):2610–2617, may 2001. doi: 10.1086/320376. URL <http://dx.doi.org/10.1086/320376>.
- Sheperd S. Doeleman, Jonathan Weintroub, Alan E. E. Rogers, Richard Plambeck, Robert Freund, Remo P. J. Tilanus, Per Friberg, Lucy M. Ziurys, James M. Moran, Brian Corey, Ken H. Young, Daniel L. Smythe, Michael Titus, Daniel P. Marrone, Roger J. Cappallo, Douglas C.-J. Bock, Geoffrey C. Bower, Richard Chamberlin, Gary R. Davis, Thomas P. Krichbaum, James Lamb, Holly Maness, Arthur E. Niell, Alan Roy, Peter Strittmatter, Daniel Werthimer, Alan R. Whitney, and David Woody. Event-horizon-scale structure in the supermassive black hole candidate at the Galactic Centre. *Nature*, 455(7209):78–80, sep 2008. doi: 10.1038/nature07245. URL <http://dx.doi.org/10.1038/nature07245>.
- Sheperd S. Doeleman, Vincent L. Fish, Avery E. Broderick, Abraham Loeb, and Alan E. E. Rogers. DETECTING FLARING STRUCTURES IN SAGITTARIUS A* WITH HIGH-FREQUENCY VLBI. *ApJ*, 695(1):59–

- 74, mar 2009. doi: 10.1088/0004-637x/695/1/59. URL <http://dx.doi.org/10.1088/0004-637x/695/1/59>.
- H Falcke and S B Markoff. Toward the event horizon—the supermassive black hole in the Galactic Center. *Class. Quantum Grav.*, 30(24):244003, nov 2013. doi: 10.1088/0264-9381/30/24/244003. URL <http://dx.doi.org/10.1088/0264-9381/30/24/244003>.
- Heino Falcke, W. M. Goss, Hiroshi Matsuo, Peter Teuben, Jun-Hui Zhao, and Robert Zylka. The Simultaneous Spectrum of Sagittarius A* from 20 Centimeters to 1 Millimeter and the Nature of the Millimeter Excess. *ApJ*, 499(2):731–734, jun 1998. doi: 10.1086/305687. URL <http://dx.doi.org/10.1086/305687>.
- V. L. Fish, S. S. Doeleman, A. E. Broderick, A. Loeb, and A. E. E. Rogers. Detecting Changing Polarization Structures in Sagittarius A* with High Frequency VLBI. *ApJ*, 706:1353–1363, December 2009. doi: 10.1088/0004-637X/706/2/1353.
- Vincent L. Fish, Sheperd S. Doeleman, Christopher Beaudoin, Ray Blundell, David E. Bolin, Geoffrey C. Bower, Richard Chamberlin, Robert Freund, Per Friberg, Mark A. Gurwell, Mareki Honma, Makoto Inoue, Thomas P. Krichbaum, James Lamb, Daniel P. Marrone, James M. Moran, Tomoaki Oyama, Richard Plambeck, Rurik Primiani, Alan E. E. Rogers, Daniel L. Smythe, Jason SooHoo, Peter Strittmatter, Remo P. J. Tilanus, Michael Titus, Jonathan Weintraub, Melvyn Wright, David Woody, Ken H. Young, and Lucy M. Ziurys. 1.3 mm WAVELENGTH VLBI OF SAGITTARIUS A*: DETECTION OF TIME-VARIABLE EMISSION ON EVENT HORIZON SCALES. *ApJ*, 727(2):L36, jan 2011. doi: 10.1088/2041-8205/727/2/l36. URL <http://dx.doi.org/10.1088/2041-8205/727/2/136>.
- Vincent L. Fish, Michael D. Johnson, Ru-Sen Lu, Sheperd S. Doeleman, Katherine L. Bouman, Daniel Zoran, William T. Freeman, Dimitrios

- Psaltis, Ramesh Narayan, Victor Pankratius, Avery E. Broderick, Carl R. Gwinn, and Laura E. Vertatschitsch. IMAGING AN EVENT HORIZON: MITIGATION OF SCATTERING TOWARD SAGITTARIUS A*. *ApJ*, 795(2):134, oct 2014. doi: 10.1088/0004-637x/795/2/134. URL <http://dx.doi.org/10.1088/0004-637x/795/2/134>.
- Vincent L. Fish, Michael D. Johnson, Sheperd S. Doeleman, Avery E. Broderick, Dimitrios Psaltis, Ru-Sen Lu, Kazunori Akiyama, Walter Alef, Juan Carlos Algaba, Keiichi Asada, Christopher Beaudoin, Alessandra Bertarini, Lindy Blackburn, Ray Blundell, Geoffrey C. Bower, Christiaan Brinkerink, Roger Cappallo, Andrew A. Chael, Richard Chamberlin, Chi-Kwan Chan, Geoffrey B. Crew, Jason Dexter, Matt Dexter, Sergio A. Dzib, Heino Falcke, Robert Freund, Per Friberg, Christopher H. Greer, Mark A. Gurwell, Paul T. P. Ho, Mareki Honma, Makoto Inoue, Tim Johannsen, Junhan Kim, Thomas P. Krichbaum, James Lamb, Jonathan León-Tavares, Abraham Loeb, Laurent Loinard, David MacMahon, Daniel P. Marrone, James M. Moran, Monika Mościbrodzka, Gisela N. Ortiz-León, Tomoaki Oyama, Feryal Özel, Richard L. Plambeck, Nicolas Pradel, Rurik A. Primiani, Alan E. E. Rogers, Katherine Rosenfeld, Helge Rottmann, Alan L. Roy, Chester Ruszczyk, Daniel L. Smythe, Jason SooHoo, Justin Spilker, Jordan Stone, Peter Strittmatter, Remo P. J. Tilanus, Michael Titus, Laura Vertatschitsch, Jan Wagner, John F. C. Wardle, Jonathan Weintraub, David Woody, Melvyn Wright, Paul Yamaguchi, André Young, Ken H. Young, J. Anton Zensus, and Lucy M. Ziurys. PERSISTENT ASYMMETRIC STRUCTURE OF SAGITTARIUS A* ON EVENT HORIZON SCALES. *ApJ*, 820(2):90, mar 2016. doi: 10.3847/0004-637x/820/2/90. URL <http://dx.doi.org/10.3847/0004-637x/820/2/90>.
- R. Genzel, R. Schödel, T. Ott, A. Eckart, T. Alexander, F. Lacombe, D. Rouan, and B. Aschenbach. Near-infrared flares from accreting gas

- around the supermassive black hole at the Galactic Centre. *Nature*, 425: 934–937, October 2003. doi: 10.1038/nature02065.
- S. Gillessen, F. Eisenhauer, T. K. Fritz, H. Bartko, K. Dodds-Eden, O. Pfuhl, T. Ott, and R. Genzel. The Orbit of the Star S2 Around SGR A* from Very Large Telescope and Keck Data. *ApJ*, 707:L114–L117, December 2009. doi: 10.1088/0004-637X/707/2/L114.
- C. Goddi, H. Falcke, M. Kramer, L. Rezzolla, C. Brinkerink, T. Bronzwaer, R. Deane, M. De Laurentis, G. Desvignes, J. R. J. Davelaar, F. Eisenhauer, R. Eatough, R. Fraga-Encinas, C. M. Fromm, S. Gillessen, A. Grenzebach, S. Issaoun, M. Janßen, R. Konoplyta, T. P. Krichbaum, R. Laing, K. Liu, R.-S. Lu, Y. Mizuno, M. Moscibrodzka, C. Müller, H. Olivares, O. Porth, O. Pfuhl, E. Ros, F. Roelofs, K. Schuster, R. Tilanus, P. Torne, I. van Bemmel, H. J. van Langevelde, N. Wex, Z. Younsi, and A. Zhidenko. BlackHoleCam: fundamental physics of the Galactic center. *ArXiv e-prints*, June 2016.
- J. Goodman and R. Narayan. The shape of a scatter-broadened image - II. Interferometric visibilities. *MNRAS*, 238(3):995–1028, jun 1989. doi: 10.1093/mnras/238.3.995. URL <http://dx.doi.org/10.1093/mnras/238.3.995>.
- C. R. Gwinn, M. D. Johnson, J. E. Reynolds, D. L. Jauncey, A. K. Tzioumis, H. Hirabayashi, H. Kobayashi, Y. Murata, P. G. Edwards, S. Dougherty, B. Carlson, D. del Rizzo, J. F. H. Quick, C. S. Flanagan, and P. M. McCulloch. Size of the Vela Pulsar's Emission Region at 18 cm Wavelength. *ApJ*, 758:7, October 2012. doi: 10.1088/0004-637X/758/1/7.
- C. R. Gwinn, Y. Y. Kovalev, M. D. Johnson, and V. A. Soglasnov. DISCOVERY OF SUBSTRUCTURE IN THE SCATTER-BROADENED IMAGE OF SGR A*. *ApJ*, 794(1):L14, sep 2014. doi: 10.1088/2041-8205/794/1/l14. URL <http://dx.doi.org/10.1088/2041-8205/794/1/l14>.

- J. P. Hamaker, J. D. Bregman, and R. J. Sault. Understanding radio polarimetry. I. Mathematical foundations. *A&AS*, 117:137–147, May 1996.
- DC Hogg, FO Guiraud, and MT Decker. Measurement of excess radio transmission length on earth-space paths. *A&A*, 95:304–307, 1981.
- T. Johannsen and D. Psaltis. Testing the No-hair Theorem with Observations in the Electromagnetic Spectrum. II. Black Hole Images. *ApJ*, 718:446–454, July 2010. doi: 10.1088/0004-637X/718/1/446.
- M. D. Johnson, V. L. Fish, S. S. Doeleman, A. E. Broderick, J. F. C. Wardle, and D. P. Marrone. Relative Astrometry of Compact Flaring Structures in Sgr A* with Polarimetric Very Long Baseline Interferometry. *ApJ*, 794:150, October 2014. doi: 10.1088/0004-637X/794/2/150.
- M. D. Johnson, V. L. Fish, S. S. Doeleman, D. P. Marrone, R. L. Plambeck, J. F. C. Wardle, K. Akiyama, K. Asada, C. Beaudoin, L. Blackburn, R. Blundell, G. C. Bower, C. Brinkerink, A. E. Broderick, R. Cappallo, A. A. Chael, G. B. Crew, J. Dexter, M. Dexter, R. Freund, P. Friberg, R. Gold, M. A. Gurwell, P. T. P. Ho, M. Honma, M. Inoue, M. Kosowsky, T. P. Krichbaum, J. Lamb, A. Loeb, R.-S. Lu, D. MacMahon, J. C. McKinney, J. M. Moran, R. Narayan, R. A. Primiani, D. Psaltis, A. E. E. Rogers, K. Rosenfeld, J. SooHoo, R. P. J. Tilanus, M. Titus, L. Vertatschitsch, J. Weintraub, M. Wright, K. H. Young, J. A. Zensus, and L. M. Ziurys. Resolved magnetic-field structure and variability near the event horizon of Sagittarius A. *Science*, 350(6265):1242–1245, dec 2015. doi: 10.1126/science.aac7087. URL <http://dx.doi.org/10.1126/science.aac7087>.
- Michael D. Johnson and Carl R. Gwinn. THEORY AND SIMULATIONS OF REFRACTIVE SUBSTRUCTURE IN RESOLVED SCATTER-BROADENED IMAGES. *ApJ*, 805(2):180, jun 2015. doi: 10.1088/0004-637x/805/2/180. URL <http://dx.doi.org/10.1088/0004-637x/805/2/180>.

- T. P. Krichbaum, D. A. Graham, A. Witzel, A. Greve, J. E. Wink, M. Grewing, F. Colomer, P. de Vicente, J. Gomez-Gonzalez, A. Baudry, and J. A. Zensus. VLBI observations of the galactic center source SGR A* at 86 GHz and 215 GHz. *A&A*, 335:L106–L110, July 1998.
- A. P. Lane. Submillimeter Transmission at South Pole. In G. Novak and R. Landsberg, editors, *Astrophysics From Antarctica*, volume 141 of *Astronomical Society of the Pacific Conference Series*, pages 289–295, 1998.
- R G Lane, A Glindemann, and J C Dainty. Simulation of a Kolmogorov phase screen. *Waves in Random Media*, 2(3):209–224, jul 1992. doi: 10.1088/0959-7174/2/3/003. URL <http://dx.doi.org/10.1088/0959-7174/2/3/003>.
- O. P. Lay. The temporal power spectrum of atmospheric fluctuations due to water vapor. *A&AS*, 122(3):535–545, may 1997. doi: 10.1051/aas:1997154. URL <http://dx.doi.org/10.1051/aas:1997154>.
- R.-S. Lu, T. P. Krichbaum, A. Eckart, S. König, D. Kunneriath, G. Witzel, A. Witzel, and J. A. Zensus. Multiwavelength VLBI observations of Sagittarius A*. *A&A*, 525:A76, January 2011. doi: 10.1051/0004-6361/200913807.
- R.-S. Lu, F. Roelofs, V. L. Fish, H. Shiokawa, S. S. Doeleman, C. F. Gammie, H. Falcke, T. P. Krichbaum, and J. A. Zensus. Imaging an Event Horizon: Mitigation of Source Variability of Sagittarius A*. *ApJ*, 817:173, February 2016. doi: 10.3847/0004-637X/817/2/173.
- Ru-Sen Lu, Avery E. Broderick, Fabien Baron, John D. Monnier, Vincent L. Fish, Sheperd S. Doeleman, and Victor Pankratius. IMAGING THE SUPERMASSIVE BLACK HOLE SHADOW AND JET BASE OF M87 WITH THE EVENT HORIZON TELESCOPE. *ApJ*, 788(2):120, may 2014. doi: 10.1088/0004-637x/788/2/120. URL <http://dx.doi.org/10.1088/0004-637x/788/2/120>.

- J.-P. Macquart and G. C. Bower. Understanding the Radio Variability of Sagittarius A*. *ApJ*, 641:302–318, April 2006. doi: 10.1086/500317.
- D. P. Marrone, F. K. Baganoff, M. R. Morris, J. M. Moran, A. M. Ghez, S. D. Hornstein, C. D. Dowell, D. J. Muñoz, M. W. Bautz, G. R. Ricker, W. N. Brandt, G. P. Garmire, J. R. Lu, K. Matthews, J.-H. Zhao, R. Rao, and G. C. Bower. An X-Ray, Infrared, and Submillimeter Flare of Sagittarius A*. *ApJ*, 682:373–383, July 2008. doi: 10.1086/588806.
- COLIN R Masson. Atmospheric effects and calibrations. In *IAU Colloq. 140: Astronomy with Millimeter and Submillimeter Wave Interferometry*, volume 59, pages 87–95, 1994.
- L. Meyer, T. Do, A. Ghez, M. R. Morris, G. Witzel, A. Eckart, G. Bélanger, and R. Schödel. A 600 Minute Near-Infrared Light Curve of Sagittarius A*. *ApJ*, 688:L17, November 2008. doi: 10.1086/593147.
- John D. Monnier. Phases in interferometry. *New Astronomy Reviews*, 51(8-9):604–616, oct 2007. doi: 10.1016/j.newar.2007.06.006. URL <http://dx.doi.org/10.1016/j.newar.2007.06.006>.
- M. Mościbrodzka, H. Falcke, H. Shiokawa, and C. F. Gammie. Observational appearance of inefficient accretion flows and jets in 3D GRMHD simulations: Application to Sagittarius A*. *A&A*, 570:A7, October 2014. doi: 10.1051/0004-6361/201424358.
- R. Narayan. The Physics of Pulsar Scintillation. *Philosophical Transactions of the Royal Society A: Mathematical Physical and Engineering Sciences*, 341(1660):151–165, oct 1992. doi: 10.1098/rsta.1992.0090. URL <http://dx.doi.org/10.1098/rsta.1992.0090>.
- R. Narayan and J. Goodman. The shape of a scatter-broadened image - I. Numerical simulations and physical principles. *MNRAS*, 238(3):963–994,

- jun 1989. doi: 10.1093/mnras/238.3.963. URL <http://dx.doi.org/10.1093/mnras/238.3.963>.
- Bojan Nikolic, Rosie C Bolton, Sarah F Graves, Richard E Hills, and John S Richer. Phase correction for ALMA with 183 GHz water vapour radiometers. *A&A*, 552:A104, 2013.
- J. E. Noordam and O. M. Smirnov. The MeqTrees software system and its use for third-generation calibration of radio interferometers. *A&A*, 524: A61, nov 2010. doi: 10.1051/0004-6361/201015013. URL <http://dx.doi.org/10.1051/0004-6361/201015013>.
- G. N. Ortiz-León, M. D. Johnson, S. S. Doeleman, L. Blackburn, V. L. Fish, L. Loinard, M. J. Reid, E. Castillo, A. A. Chael, A. Hernández-Gómez, D. Hughes, J. León-Tavares, R.-S. Lu, A. Montaña, G. Narayanan, K. Rosenfeld, D. Sánchez, F. P. Schloerb, Z.-q. Shen, H. Shiokawa, J. SooHoo, and L. Vertatschitsch. The Intrinsic Shape of Sagittarius A* at 3.5-mm Wavelength. *ArXiv e-prints*, jan 2016.
- J.R. Pardo, J. Cernicharo, and E. Serabyn. Atmospheric transmission at microwaves (ATM): an improved model for millimeter/submillimeter applications. *IEEE Trans. Antennas Propagat.*, 49(12):1683–1694, 2001. doi: 10.1109/8.982447. URL <http://dx.doi.org/10.1109/8.982447>.
- A. Popping and R. Braun. The standing wave phenomenon in radio telescopes. *A&A*, 479(3):903–913, mar 2008. doi: 10.1051/0004-6361:20079122. URL <http://dx.doi.org/10.1051/0004-6361:20079122>.
- D. Psaltis, F. Özel, C.-K. Chan, and D. P. Marrone. A General Relativistic Null Hypothesis Test with Event Horizon Telescope Observations of the Black Hole Shadow in Sgr A*. *ApJ*, 814:115, December 2015. doi: 10.1088/0004-637X/814/2/115.

- Dimitrios Psaltis, Norbert Wex, and Michael Kramer. A QUANTITATIVE TEST OF THE NO-HAIR THEOREM WITH Sgr A* USING STARS PULSARS AND THE EVENT HORIZON TELESCOPE. *ApJ*, 818(2):121, feb 2016. doi: 10.3847/0004-637x/818/2/121. URL <http://dx.doi.org/10.3847/0004-637x/818/2/121>.
- S. J. Radford and M. A. Holdaway. Atmospheric conditions at a site for submillimeter-wavelength astronomy. In T. G. Phillips, editor, *Advanced Technology MMW, Radio, and Terahertz Telescopes*, volume 3357 of Proc. SPIE, pages 486–494, jul 1998.
- Alan E. E. Rogers, Sheperd S. Doeleman, and James M. Moran. Fringe detection methods for very long baseline arrays. *AJ*, 109:1391, mar 1995. doi: 10.1086/117371. URL <http://dx.doi.org/10.1086/117371>.
- E. Serabyn, J. Carlstrom, O. Lay, D. C. Lis, T. R. Hunter, J. H. Lacy, and R. E. Hills. High-Frequency Measurements of the Spectrum of Sagittarius A*. *ApJ*, 490(1):L77–L81, nov 1997. doi: 10.1086/311010. URL <http://dx.doi.org/10.1086/311010>.
- E. Serabyn, E. W. Weisstein, D. C. Lis, and J. R. Pardo. Submillimeter Fourier-transform spectrometer measurements of atmospheric opacity above Mauna Kea. *Appl. Opt.*, 37(12):2185, apr 1998. doi: 10.1364/ao.37.002185. URL <http://dx.doi.org/10.1364/ao.37.002185>.
- Z.-Q. Shen, K. Y. Lo, M.-C. Liang, P. T. P. Ho, and J.-H. Zhao. A size of \sim 1AU for the radio source Sgr A* at the centre of the Milky Way. *Nature*, 438:62–64, November 2005. doi: 10.1038/nature04205.
- O. M. Smirnov. Revisiting the radio interferometer measurement equation. *A&A*, 527:A106, 2011a. doi: 10.1051/0004-6361/201016082. URL <http://dx.doi.org/10.1051/0004-6361/201016082>.

- O. M. Smirnov. Revisiting the radio interferometer measurement equation. *A&A*, 527:A107, 2011b. doi: 10.1051/0004-6361/201116434. URL <http://dx.doi.org/10.1051/0004-6361/201116434>.
- O. M. Smirnov. Revisiting the radio interferometer measurement equation. *A&A*, 527:A108, 2011c. doi: 10.1051/0004-6361/201116435. URL <http://dx.doi.org/10.1051/0004-6361/201116435>.
- R. Takahashi. Shapes and Positions of Black Hole Shadows in Accretion Disks and Spin Parameters of Black Holes. *ApJ*, 611:996–1004, August 2004. doi: 10.1086/422403.
- V. I. Tatarskii. The effects of the turbulent atmosphere on wave propagation. 1971.
- A. R. Thompson, J. M. Moran, and G. W. Swenson, Jr. *Interferometry and Synthesis in Radio Astronomy, 2nd Edition*. 2001.
- R. N. Treuhaft and G. E. Lanyi. The effect of the dynamic wet troposphere on radio interferometric measurements. *Radio Science*, 22(2):251–265, mar 1987. doi: 10.1029/rs022i002p00251. URL <http://dx.doi.org/10.1029/rs022i002p00251>.
- J. M. Wrobel and R. C. Walker. Sensitivity. 180:171, 1999.
- F. Yusef-Zadeh, D. Roberts, M. Wardle, C. O. Heinke, and G. C. Bower. Flaring Activity of Sagittarius A* at 43 and 22 GHz: Evidence for Expanding Hot Plasma. *ApJ*, 650:189–194, October 2006. doi: 10.1086/506375.